ABSTRACT

KIM, CHANG HYEUK. A Study of Monochromatic X-ray Area Beam for Application in Diffraction Enhanced Imaging. (Under the direction of Dr. Mohamed A. Bourham.)

Synchrotron-based Diffraction Enhanced Imaging (DEI) system has shown improved contrast images on low attenuation material. In a previous DEI study great potential to detect earlier stage breast cancer was reported. However, to apply DEI technique at the clinical level, a synchrotron source is not feasible for clinically-approved systems due to the size of the accelerator, and hence a compact x-ray source that can replace synchrotron is desirable. Development of an x-ray source compatible to synchrotron radiation is an essential part for a clinical DEI system. Some important features for the design of an x-ray source, based on synchrotron radiation, are the photon flux and beam collimation. The NCSU research group suggested a wide-beam x-ray source, which consists of concentric circular filaments producing electron flux onto a cylindrically-shaped oxygen-free copper stationary target with a thin layer of Molybdenum for x-ray production. This source design emphasizes large field of view, which can eliminate the line by line scanning process experienced in a DEI experimental setup. In this study, the proof of principle model of a wide beam x-ray source was used to study for control electron trajectory of the concentric filaments design, calculations of the produced x-ray flux, simulation of the DEI imaging, and estimation of the operation time with target's active cooling system. The DEI images from the electron distribution were computationally generated by adopting a monochromator and an analyzer with a computationally generated dual cylindrical object. The image simulation showed that the wide-beam x-ray source based DEI images are highly dependent on the electron distribution at the target. Uniform electron distribution by electron trajectory optimization is carried out through independent powering of the filaments inside the focusing cup. For

higher electron beam current the x-ray flux satisfies obtaining a successful DEI image scan, but such high current increases the heat loading on the target. The target cooling with a contact cold finger does not provide sufficient thermal management, and hence not enough scanning time. The impinging jet nozzle cooling option was investigated to maximize convective heat transfer, and has shown feasible thermal management and adequate operation time for DEI imaging.

A Study of Monochromatic X-ray Area Beam for Application in Diffraction Enhanced Imaging

by

Chang Hyeuk Kim

A dissertation submitted to the Graduate Faculty of
North Carolina State University
in partial fulfillment of the
requirements for the Degree of
Doctor of Philosophy

Nuclear Engineering

Raleigh, North Carolina

2007

Approved by:

Dr. Mohamed A. Bourham Chair of Advisory Committee	Dr. J. Michael Doster
Dr. Man-Sung Yim	Dr. David S. Lalush

DEDICATION

For Sujin

BIOGRAPHY

I was born on May 22, 1976 in GwangJu, South Korea. I grew up within Gwangju with parents, Woo-Jeon Kim and Kyoung-Sook Beck, and my sister, Nu-Lee Kim. After my graduation from Gwnagju In-Sung high school, I started my college studies in 1994 at Chosun University in Nuclear Engineering. I joined the Korean Air Force in 1995 for military service as a missile launcher operator in the Air Defense Artillery. After two and half years of military service, I returned to school in 1998. I obtained my B.S. degree in 2002 then joined the graduate program in the Department of Nuclear Engineering at North Carolina State University. I joined the x-ray research group in 2003 and earned M.S degree in 2004 on the study of an area x-ray source for Diffraction Enhanced Imaging for clinical and industrial applications. I am married to Sujin Oh in 2005 and we have a daughter, Ellie Hyobin Kim.

ACKNOWLEGEMENTS

I would like to express my gratitude to Dr. Mohamed A. Bourham. He has been my academic advisor and good example to me as a researcher. Without his kindly and sincere guidance, I could not complete this dissertation. I am also grateful to my committee members, Dr. J. Michael Doster, Dr. Man-Sung Yim and Dr. David S. Lalush for their help and discussions. Dr. Doster has provided substantial help in the target heat management and thermal analysis. I greatly acknowledge the help and support I received from the Department of Nuclear Engineering during the course of my study. Special thanks to Dr. Man-Sung Yim for his invaluable guidance during my graduate study. Lastly, I would like to express my thankfulness to my wife, Sujin for believing in me and being with me.

TABLE OF CONTENTS

page

LIST OF FIGURES

page

LIST OF TABLES

page

Chapter 1 Introduction

Diffraction Enhanced Imaging was initially proposed by Dean Chapman in 1998 [1], followed by an experimental setup performed with the synchrotron radiation source at National Synchrotron Light Source in Brookhaven National Laboratory. The DEI experiment has shown good contrast images at lower radiation dose for materials with small x-ray attenuation coefficient [2]. The features of the DEI method were considered as a new imaging modality for clinical and industrial fields. In clinical application, it is mostly desired for mammography because of the lower exposure rate and the higher contrast images.

The DEI system adopts a very narrow x-ray energy range to make successful x-ray diffraction on the analyzer crystal. A monochromator is utilized to select the energy range of the x-ray from the provided raw synchrotron radiation, called white radiation [3]. The general DEI experimental setup is shown in Figure 1.1 in which the incident beam passes to a double-crystal Si [333] monochromator then towards the object, and the exiting beam from the object passes to a Si [333] crystal analyzer, diffracted towards the detector. Most of the x-rays, which do not meet the monochromator conditions, are absorbed by the monochromator and hence the x-ray flux leaving the monochromator is lower than the white radiation. And, the monochromatized beam is also strongly collimated. According to this monochromatization process, the radiation dose to the object is relatively lower than that of conventional x-ray radiography.

The main obstacle of the DEI application for medical use in a reasonable medical facility, or at the clinical level, is the need for a synchrotron source, which is not a feasible component for practical employment of DEI systems, considering the size and cost of the synchrotron facility. An alternative method would be the use of conventional x-ray tubes, but

such tubes have lower flux and produce a fan-shaped beam and such features do not meet the requirements for the quality of the x-ray needed for DEI systems.

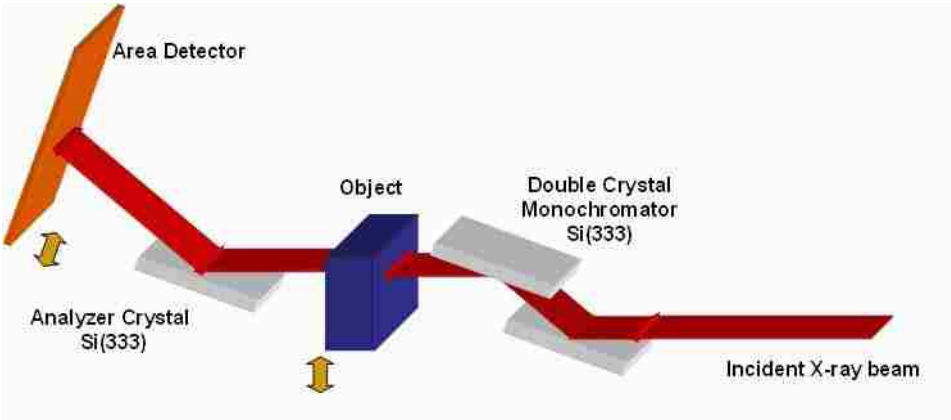

Figure 1 . 1 The general DEI experiment setup

The NCSU research group suggested a wide beam area x-ray source, which can provide x-ray with flux comparable to synchrotron source [4]. This proposed x-ray source should meet specific conditions; appropriate x-ray energy range for mammography, higher x-ray flux and large field of view. A cylindrical shape of stationary oxygen-free copper target with a layer of molybdenum was proposed. The molybdenum layer will generate the 18 keV characteristic x-ray, which is preferred for mammography due to its low energy. Most of the electron beam energy will be transferred to heat on the target, which necessitates target thermal management for high beam currents required to produce high photon flux. In most conventional x-ray tubes, a rotating target is used to spread the heat over larger surface and thus reduce heat loading. In case of stationary targets in some x-ray tubes, a passive cooling system is employed either using air or oil cooling of the target. A rotating target is not feasible for a high-beam-current large area x-ray source and thus a stationary target is

desirable and hence target active cooling will be necessary for the proposed wide beam x-ray source.

1 Diffraction Enhanced Imaging

After Roentgen discovered x-ray in 1895, x-ray radiography was used in many fields, for clinical and industrial purposes. The x-ray projection radiography is still treated as a basic imaging method in medical field. It has many advantages, a simple scanning process, high contrast images, and low cost of examination. The superposition of images, and lower contrast images of some materials, is mentioned as a disadvantage of conventional x-ray imaging systems. Cancerous tissues and joint cartilage are not shown very well in conventional radiographs, as well as in the Computed Tomography (CT) due to their respective attenuation coefficient at the used range of x-ray. In general, conventional radiography and CT machines use tungsten targets, which generate $K_{\alpha 1}$ characteristic x-ray at about 59.32keV energy. The attenuation coefficients of these materials in this energy range are very close to the surrounded material, which reduces the contrast and consequently the readability of the radiographs. Other imaging modalities, other than using x-rays, are used such as Magnetic resonance Imaging (MRI) or Ultrasound.

Diffraction Enhanced Imaging is a type of projection radiography and therefore it still has a limitation on the pileup of objects in the imaging, however some research is ongoing to develop tomographic imaging with DEI [5]. As mentioned earlier, the DEI produces images of higher contrast for materials with small attenuation coefficient, as compared to conventional and digital radiography. The attenuation coefficient of all materials is small at the x-ray high energy region with higher attenuation at the a low energy range, and thus

lower energy x-ray is selected for DEI systems. The main interaction at the lower x-ray energy range is the photoelectric effect, which has a probability proportional to Z/E^{3}, where Z is the atomic number of the material and E is the photon energy. Therefore, the difference in the attenuation coefficient on the lower energy produces better contrast at the DEI absorption image. The other feature of DEI is the use of an analyzer crystal to diffract x-rays, and hence, the recorded x-ray contains selected information about the object. Consequently, the DEI refraction image shows only one physical phenomenon between x-ray and objects, x-ray refraction angle; which would appear as "image blurring" in general projection radiography.

1.1 Synchrotron based DEI

In the DEI experiment setup by Dean Chapman et al using a synchrotron source, three crystals were used in the setup [1]. The incident x-ray beam falls on double crystal Si [333] monochromators, the exited beam traverses through the object then to a third Si [333] crystal that acts as an analyzer. These crystals diffract the x-ray by the Bragg's law [6] thus there are x-ray losses on the x-ray path way and the x-ray flux drops down by a factor of 4 during the monochromatization [3]. Due to expected drop in x-ray flux, the use of synchrotron source at high photon flux was experimented with the white radiation has a spectrum that is almost uniform through the entire energy range. The monochromator selects a specific x-ray energy from the white radiation. It is also important to mention that a synchrotron source can provide a well-collimated x-ray beam, which implies that a synchrotron source would be the best to use for DEI to provide high quality images. The difficulty in using a synchrotron source is in the cost and the size of the accelerator that is unfeasible for clinical applications

in major medical facilities or hospitals.

1.2 X-ray source based DEI

As previously mentioned, a DEI system should employ an x-ray source capable of producing high flux compatible with synchrotron sources, as well as a strongly collimated beam. Typical conventional x-ray tubes have relatively low x-ray flux. When used for mammography, a longer scanning time would be necessary to obtain appropriate images. Additionally, such tubes have very small focal spot and large imaging area, and thus the produced x-ray is divergent and not collimated. To use such source for a DEI system, the recorded x-ray shape on the imaging plate will be tiny as it follows the small effective focal spot of the x-ray tube. Hence, using a conventional x-ray source is not a solution for the DEI application unless the source is modified to provide an area beam at high x-ray flux.

2 Wide beam x-ray source

The characteristics of a typical x-ray tube are not feasible for use in DEI application without serious consideration regarding x-ray flux, effective focal spot and size of the beam. A wide beam x-ray source can correct the defects of a typical x-ray source. First, higher electron beam current can provide higher x-ray flux. A typical x-ray tube has relatively short filaments for thermionic emission. For a wide beam source, three concentric filaments were considered to increase production of electrons and provide a higher electron beam current. Second, a stationary target with large illumination area is chosen to provide a larger focal spot. Third, a target active cooling system is employed to manage thermal loading and allow for longer operation time sufficient to obtain images. In this study, the concept of a wide

beam x-ray source, a proof-of-principle system, is computationally studied. A set of computer codes were used, such as SIMION 3D, MCNP5, Matlab, COMSOL Multiphysics, and ANSYS CFX, with developed input codes for geometry and DEI imaging.

2.1 Steering electron trajectories

The wide beam x-ray source uses three concentric circular filaments to generate a large focal area. Electrons are produced by thermionic emission and accelerated towards the grounded target by the electric field between the focusing cup and the target. Concentric filaments may be all connected together and powered by same current and voltage or individually powered to provide independent control on electron flux and distribution of the beam particles on the target. The focusing cup may be on same negative accelerating potentials as the cathode. An optimization of the electron trajectories and their distribution is investigated in this dissertation.

2.2 X-ray flux

The x-ray flux from the wide beam source should be compatible with the synchrotron radiation flux "white beam" in order to apply the DEI technique. The x-ray flux is affected by the electron beam current and the x-ray window material that acts as a final x-ray filter. The x-ray window should stand high vacuum conditions while meeting other requirements such as eliminating bremsstrahlung radiation, which only contributes to the radiation dose while minimizing attenuation of the characteristic x-rays that are used to obtain images [7].

2.3 DEI Images

The DEI image quality of the wide beam x-ray source depends on the electron distribution on the target, known as the actual focal area. Therefore, the final image can change by optimization techniques for electron distribution and steering electron trajectories. In this study, a phantom consisted of two materials, aluminum oxides and nylon, was computationally studied for simulation of DEI images from the area x-ray source. These materials were selected as representation of microcalcification on breast cancer and normal tissue.

2.4 Heat removal

Accelerated electrons in the x-ray system impact and deposit their energy on the target, thus the target temperature rises as a result of transferring electron energy to heat on the target. Conventional x-ray sources do not have serious heat removal problems because they either use a rotating target or a cooling system. Additionally, they use relatively low electron beam current and thus thermal loading of the target is not an issue. This is not the case for an area x-ray source, in which the required electron beam current is up to 3A and if operating at 60kVp then the target heat loading would be 180kW. In this study, target thermal management is considered to ensure safe operation of such high beam current source for a time sufficient to obtain DEI images without target deterioration, melting or even evaporation at such high heat flux. Conduction and convective heat transfer were considered in this study, as well as the use of a contact cold finger (at liquid nitrogen temperature) and circulation of a coolant.

References

[1] Chapman D, Thomlinson W, Johnston RE, et al., Diffraction enhanced x-ray imaging, Phys. Med. Bio. 42: 2015-2025, 1997.

[2] Pisano ED, Johnston RE, Chapman D, Geradts J, Iacocca MV, Livasy CA, Washburn DB, Sayers DE, Zhong Z, Kiss MZ, Thomlinson WC. Human Breast Cancer Specimens: Diffraction-enhanced Imaging with Histologic Correlation - Improved Conspicuity of Lesion Detail Compared with Digital Radiography, Radiology 414(3), 895-901, 2000.

[3] Zhong Z., Thomlinson W., Chapman D., Sayers D. Implementation of Diffraction Enhanced Imaging at the NSLS and APS, Nuclear Instrument and Method in Physics Research A 447: 556-568, 2000.

[4] E. Pisano, E. Johnson, D. Chapman , Z. Zhong, D. Sayers, K. Verghese, J.M. Doster, M.A. Bourham and M. Yaffee, "Clinical Diffraction Enhanced Mammography Unit", NCSU and UNC-CH Invention Disclosure, July 2000, NCSU File Number 01-59.

[5] Dilmanian F. A., Zhong Z., B Ren, XY Wu, L D Chapman, I Orion, W C Thomlinson, Computed tomography of x-ray index of refraction using the diffraction enhanced imaging method. Phys. Med. Biol. 45: 933-946, 2000.

[6] Andre Authier, Dynamical theory of x-ray diffraction, International Union of Crystallography, OXFORD University Press (2001).

[7] Jerrold T. Bushberg et al, The Essential Physics of Medical Imaging, 2nd ed., Lippincott Williams & Wilkins (2002), Baltimore Maryland

Chapter 2 A wide-beam X-ray source suitable for diffraction enhanced imaging applications

Available online at www.sciencedirect.com
ScienceDirect
Nuclear Instruments and Methods in Physics Research A 566 (2006) 713–721
NUCLEAR INSTRUMENTS & METHODS IN PHYSICS RESEARCH Section A
www.elsevier.com/locate/nima

A wide-beam X-ray source suitable for diffraction enhanced imaging applications

Chang H. Kim*, Mohamed A. Bourham, J. Michael Doster

Department of Nuclear Engineering, North Carolina State University, Raleigh, NC 27695-7909, USA

Received 10 February 2006; received in revised form 5 July 2006; accepted 16 July 2006
Available online 11 August 2006

Abstract

Research in diffraction-enhanced imaging (DEI), using a synchrotron source with an X-ray flux of 1.4×10^{12} ph/mm^2/s, has shown strong potential in obtaining high-resolution images as compared to conventional radiographs. This research investigates the feasibility of developing a large area circular X-ray source with fluxes comparable to a synchrotron source. The source should be capable of integration into a compact system with peak powers not to exceed 200 kW to be feasible for use in a major medical facility, industrial complex or screening facility (such as cargo or airport). A computational study of a circular concentric filament wide-beam area X-ray source has been investigated in this research. The design features are based on generating electrons from three concentric circular filaments to provide an area electron flux, with a 60 kV accelerating potential and a beam current of up to 3 A. The X-ray target is a grounded stationary oxygen-free copper target with a layer of molybdenum. This target feature differs from standard rotating X-ray targets in conventional X-ray systems. Studies of electron trajectories and their distribution on the target were conducted using the SIMION 3D code. Heat loading and thermal management were studied using heat transfer modules from the coupled FEMLAB multi-physics and MATLAB codes. The Monte Carlo code MCNP 5 was used to obtain the X-ray flux and energy distribution for aluminum and beryllium windows. This computational study shows that this target configuration generates X-rays with photon flux comparable to synchrotron source and sufficient for DEI applications. The maximum target temperature rise is 1357 K after 70 s when cooling the back of the target to liquid nitrogen temperature using cold finger contact, and 325 K for an invaded target, in which liquid nitrogen circulates inside the target.

PACS: 41.50.+h; 41.85.Ew; 32.30.Rj; 87.59.−e

Keywords: Diffraction enhanced imaging; Electron trajectory; Heat conduction; Characteristic X-ray

1. Introduction

Although development of digital mammography has enabled better diagnosis with the integration of advanced image digital processing [1], images produced through diffraction-enhanced imaging techniques have proven to be of high quality as image scattering is eliminated [2–4]. In the preliminary work of Chapman et al., in which the highly collimated synchrotron source from X15A beamline of the National Synchrotron Light Source (NSLS) in Brookhaven National Laboratory was used, the obtained DEI images have shown details and characteristics not detected by conventional imaging [2–5]. In Chapman et al. DEI setup, the system employed Si(3 3 3) crystals for producing monochromatic and diffracted X-ray beams, which is refracted through a very small angular deflection of the order of micro-radian. This arrangement made it possible to obtain higher contrast images from the same object. However, the use of a synchrotron source necessitates having a DEI system close to a major synchrotron facility. A clinically approved DEI system, which may be installed in major hospitals, would need a new X-ray source that can provide a substitute for a synchrotron source. Other applications of high-resolution enhanced radiography may be extended to material science research and crystallography such as 3-D

*Corresponding author. Tel.: +1 919 645 8015.
E-mail address: Chkim4@unity.ncsu.edu (C.H. Kim).

0168-9002/$ - see front matter © 2006 Elsevier B.V. All rights reserved.
doi:10.1016/j.nima.2006.07.041

mapping of composite materials, grains in polycrystalline materials, distribution of elements in cells and imaging of sprays [6,7]. Additionally, there would be other potential industrial applications such as advanced radiography for cargo and parcel screening with enhanced resolution for active interrogation techniques.

The purpose of this study is to investigate the feasibility of developing a new compact size area X-ray source capable of producing photon fluxes of sufficient intensity and quality needed for diffraction-enhanced imaging without using a synchrotron source. This computational study is a first step from laboratory testing version towards developing a proto-type system as a clinically approved DEI system for medical radiology followed by scalability to other applications. The desirable features of an area X-ray generator compatible to a synchrotron source to satisfy DEI requirements are [10–12]:

- Peak electric power less than 200 kW, 3 A beam current at 60 kVp.
- High target flux ($\sim 10^{12}$ ph/mm^2/s) to be compatible to the synchrotron source target flux.
- Output X-ray beam collimated over a 100 cm^2 area.
- Reasonable operation time (5–10 s).
- Stationary target assembly and concentric or spiral filament configuration.

The major aspects of this study are the electrostatic analysis and electron trajectories and their distribution, the thermal analysis and target heat loading for appropriate operation time, and investigation of X-ray energies and X-ray flux at the extraction window of the system.

2. General considerations

The white beam from the X15A beamline at NSLS delivers a target flux of 1.4×10^{12} ph/s/mm^2/keV at 18 keV. After the beam went through Si[1 1 1] double crystal monochromator, the flux drops $\sim 10^7$ ph/s/mm^2/keV at 18 keV. Typical scanning time to acquire an image with such synchrotron beam is in the range of 4–200 s [11]. A conventional X-ray tube, operating with thermionic emission filaments, may be used to substitute for the X-ray source. However, conventional X-ray tubes have continuous spectra and low beam intensity as compared to synchrotron sources [8]. The Bremsstrahlung radiation from a conventional X-ray tube delivers unnecessary radiation dose to the patient, and is not useful for DEI applications. Moreover, the low beam intensity increases the scan time, which is estimated to be between 1000 and 10,000 s for a conventional source. In addition, a collimated area X-ray beam can provide area magnification for DEI applications. A conventional X-ray tube typically operates with a 0.3–0.4 mm focal spot [9]. For a clinically approved DEI mammography unit, the dimension of the beam in the sagittal direction will be 150 mm to get a full field of view.

Several concepts for a new X-ray source were proposed by a North Carolina State University research group in collaboration with a University of North Carolina Chapel Hill Radiology group and others, such as the shaped-target multi-filament concept, the high-current beam steering concept and the cold cathode field emission concept [10,11]. Of these, the shaped-target multi-filament concept has the most attractive features. In this concept, the source design is based on a tilted stationary molybdenum target with the target's surface shaped in a log-spiral. Filaments are arranged as an array of line filaments, with each filament assembly composed of the individual line filaments and corresponding focus cups. Total emission current of the filament array can be as high as 3 A, which will deliver a total power of 180 kW to the target at 60 kVp operation. The illumination area for this concept is 150×150 mm, however, a 50×50 mm prototype was proposed [12]. An evolution from this concept is the area X-ray source using concentric circular filaments and a stationary tilted oxygen-free copper target with a thin layer of molybdenum. This proposed target configuration would allow for better thermal management, as the target body is copper.

Increasing the accelerating potential produces higher X-ray intensity, which includes higher Bremsstrahlung in the X-ray spectrum. The higher Bremsstrahlung in the X-ray spectrum may also produce higher radiation dose to patient. The generated Bremsstrahlung radiation could be reduced or eliminated through the use of aluminum or beryllium filtering windows. Increasing the electron beam current, which depends on electron emission area from the filament, is another means by which the X-ray intensity could be increased. The typical X-ray tube uses a very small line filament, which acts as a point source not exceeding the area of the target. Concentric circular filaments increase the emission area over the standard spot-size filament source. The large electron emission area produces higher electron beam current, and higher electron flux, thus increasing the number of electrons illuminating the target surface. Both increasing accelerating potential and a larger electron emission area, result in increased heat loading of the X-ray target. The heat loading would exceed the cooling capacity of typical X-ray tubes, which usually use a rotating target to spread the heat loading over the rotating area, or an air-cooling system. Therefore, a concentric filament X-ray source operating at higher beam currents up to 3 A will necessitate the use of an active cooling system for heat removal.

For this study, the designed area X-ray generator is composed of a stationary target made of oxygen-free copper with a thin molybdenum layer, a filament assembly composed of three concentric circular filaments, an active cooling system for the target and the overall housing of the source assembly. The core of this research is to investigate the source electrostatics and generation of the electrons and their trajectories, target thermal loading and thermal management and X-ray generation. Electron trajectories and their distribution in the system are determined by the

geometry of the anode and cathode, and the form of electron acceleration. Analysis of electron trajectories and their distribution is conducted using SIMION 3D [13]. As accelerated electrons impact on the target most of their kinetic energy is converted to heat, raising the target temperature (which may exceed its melt temperature) and limits the operational time. For this purpose thermal calculations are performed using the coupled FEMLAB multi-physics and MATLAB codes. The quality and intensity of the produced X-rays are related to the target material and the electron accelerating potential, the Monte Carlo code MCNP 5 has been used for this analysis [14 16].

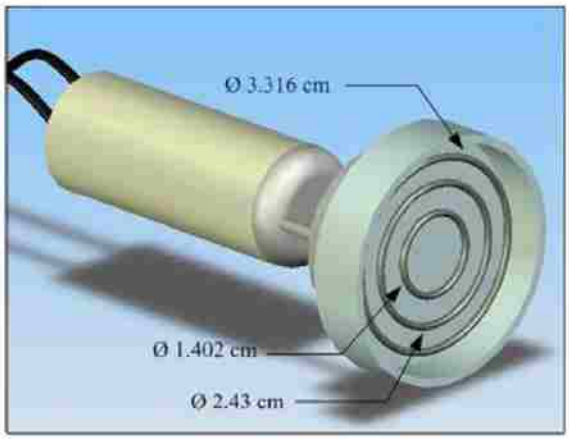

Fig. 1. Illustration of the filament assembly showing the three concentric filaments inside the filament cup.

Table 1
Parameters of the circular filaments

Filaments material: tungsten	Radius (cm)	Total length (cm)
Inner	0.701	4.404
Middle	1.215	7.634
Outer	1.658	10.417

3. Filament-target design

Three concentric circular filaments provide the required area magnification necessary for a DEI system. The total length of the filament array is about 22.5 cm, which is about 50 times longer than a filament in a conventional X-ray source. Fig. 1 shows an illustration of the filament assembly. The design parameters are shown in Table 1. The target is made of oxygen-free copper covered with a thin (<1.0 mm thick) molybdenum layer via sintering, however, other techniques such as plasma sputter deposition could be used to manufacture such targets. The molybdenum surface area is 6.157 cm^2. Fig. 2 shows the target geometry, and the target parameters are shown in Table 2 [17].

4. Simulation considerations

4.1. Electrostatics and particle trajectories simulation

Electron trajectories and particle distributions are simulated using the SIMION code assuming a 22.5° take off angle. The simulation allows for varying the electric field configuration, and a floating or non-floating filament cup base (backing plate). The power supply for the filaments is separate from the high-voltage supply, which supplies the accelerating potential between the cathode and the target. The filament base cup is set at negative potential and the X-ray target is grounded. The filament supply is floating, however, if desired one of the filament leads may be connected to the focusing cup such that they together work as a cathode, or the filament may have a high-voltage connection different from the cup potential and its supply current float on top of the high voltage. Fig. 3 illustrates

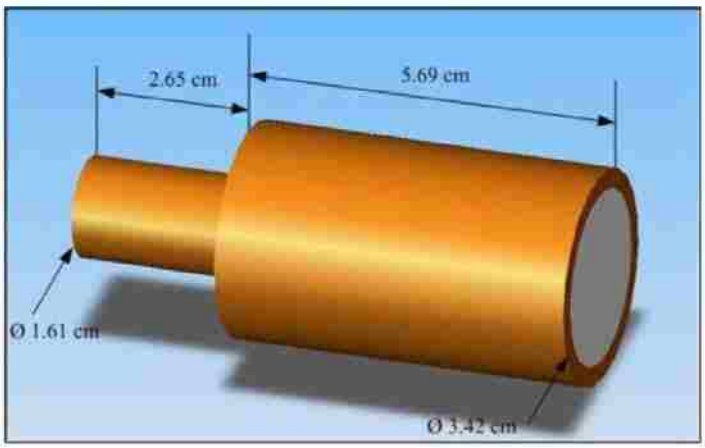

Fig. 2. Geometry of the stationary target showing the copper body and molybdenum layer.

Table 2
Stationary target parameters and thermal properties [17]

	Radius (cm)	Length (cm)	Thermal conductivity (W/cm K)	Melting point (K)
Cu Body	1.71	5.69	1.48	1357
Mo layer	1.40	<0.1	4.01	2896

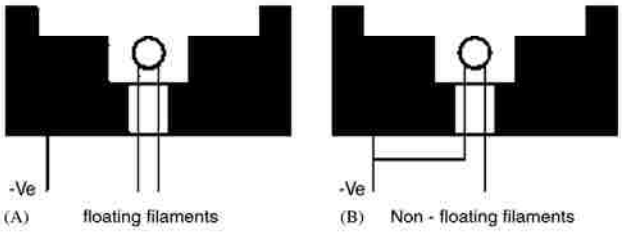

Fig. 3. Floating and non-floating filament configurations.

the configuration of the concentric filament and focusing cup assembly for the floating and non-floating (biased) options.

4.2. Thermal analysis simulation

The main heat transfer mechanism in the thermal simulation is conduction, although the actual target would emit some heat via radiation as the entire source is under vacuum. In this simulation the target front receives the inward heat flux from the electron beam, the back of the target is maintained at liquid nitrogen temperature, and the target body is assumed thermally insulated with vacuum boundaries. The properties of the target material and its geometrical shape are important factors in the thermal conduction analysis. The target is a thin (< 1 mm thick) layer of molybdenum on top of an oxygen-free cylindrical copper block. As molybdenum's melting point (2623 °C) is much greater than that of copper (1085 °C), the copper block will reach its melting point before the molybdenum if the heat loading is excessive. As a result, in these simulations the thermal resistance of the thin molybdenum layer was ignored. To perform the thermal analysis, electron beam energy and distribution at the surface of the target are used as inputs to the 3-D finite element code FEMLAB. The option of the filament connected to the backing plate acting as the cathode at −60 kV was chosen as the test case because it shows the least particle loss and the best focusing of the beam on the target. Four beam current test cases were considered, 3, 30, 300 mA, and 3 A. In all four cases, the spatial distribution of the target's temperature is obtained as a function of time, with the limiting factor set to the time-to-melt of the copper surface facing the incoming electron beam.

4.3. Characteristic X-ray simulation

The MCNP 5 Monte Carlo code has been used to calculate X-ray production and radiation dose at the extraction window. The K-shell characteristic X-rays for a molybdenum target are the $K_{\alpha 1}$ (17.48 keV), $K_{\alpha 2}$ (17.37 keV) and $K_{\beta 1}$ (19.61 keV). The X-ray intensity at the extraction window depends on the window material and its thickness. Two window materials, aluminum and beryllium, are used in this simulation with three different window thicknesses of 0.1, 0.05 and 0.01 mm for each. The selection of these two window materials and their respective thickness are intended to optimize the maximum flux of the $K_{\alpha 1}$ and $K_{\alpha 2}$ lines, and possibly the $K_{\beta 1}$ line too. It is also important in determining the optimal window design that could support such a thin large area window subject to the high vacuum condition without breaking or failure.

5. Simulation results

5.1. Electron distribution on the target

Simulation of the first option, in which the filament acts as a cathode and is biased by negative 12 Vp while the backing plate (filament cup) is at negative 60 kVp, results in an electron distribution on the target, which is almost uniform as shown in Fig. 4. However, the diverging electric field results in electron trajectories, which miss the target surface. Although target illumination is uniform and reasonable for the production of an area beam, the expected X-ray intensity is low. Fig. 5 shows the electron deposition distribution on the target surface. This option could be used for generating an area X-ray beam by lining the interior of the housing with lead to overcome shielding problems emanating from diverging electrons, and by increasing beam current to increase X-ray intensity. Increasing the beam current could be accomplished by

increased thermionic emission from the filament, which may lead to either shorter filament lifetime or filament failure at high temperatures; or by increasing the acceleration potential at same beam current, which makes the entire system impractical.

In the simulation of the second option, in which the filament acts as the cathode at −60 kVp and is connected to the focusing cup, the loss of electrons is minimal, as shown in Fig. 6, and their distribution on the target is nearly uniform except for a peak at the center of the target, as shown in Fig. 7. The hotspot could be filtered out via X-ray optics or by further optimization in this configuration.

5.2. Target thermal loading

Because of the assumption that the back of the target is maintained at liquid nitrogen temperature (liquid nitrogen contacted target), and the target body is thermally insulated, the initial target temperature was set for all cases to 77 K assuming the target is already cooled prior to operation. The heat flux on the surface of the target is obtained from the SIMION simulation electron distribution and transient thermal analysis was performed using FEMLAB. The maximum temperature of the target's surface reaches 270 K in 300 s for a 300 mA beam current, which indicates that the operation with such beam current is almost near steady state. For lower beam currents of 3 and 30 mA, the maximum temperatures are 77 and 90 K in 100 s, respectively (almost maintained at liquid nitrogen temperature). Therefore, in the case of 300 mA, with 270 K reached in 300 s the system could serve enough operation time without heat loading concerns, however, to reach sufficient target flux, a 3 A beam current would be required. In the 3 A beam current case, the target temperature reaches 1357 K in 70 s, which is the melting point of copper. Thus, the liquid nitrogen contacted target configuration

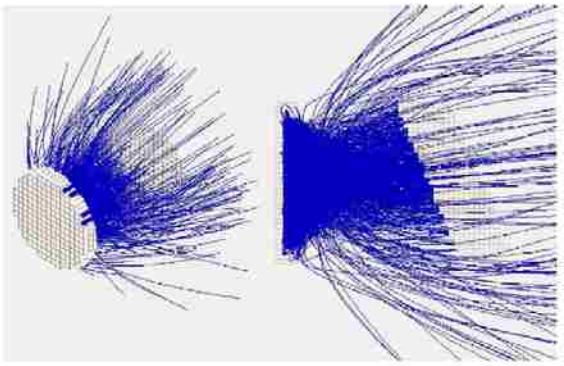

Fig. 4. Electron trajectories with −60 kVp focusing cup and filaments at −12 Vp.

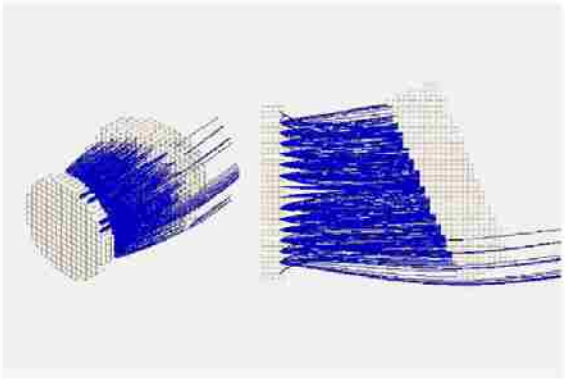

Fig. 6. Electron trajectories with −60 kVp focusing cup and filaments.

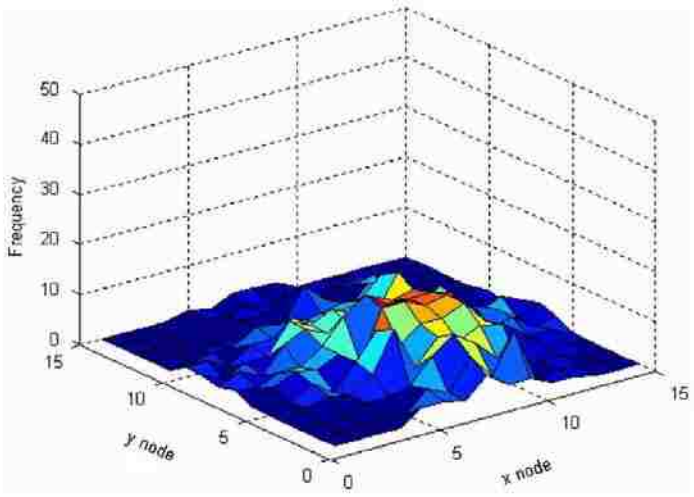

Fig. 5. Electron deposition distributions with −60 kVp focusing cup and filaments at −12 Vp.

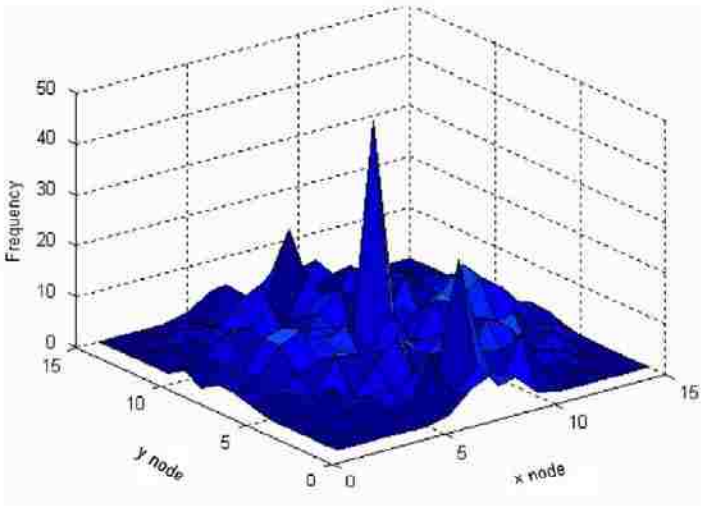

Fig. 7. Electron deposition distributions with −60 kVp focusing cup and filaments.

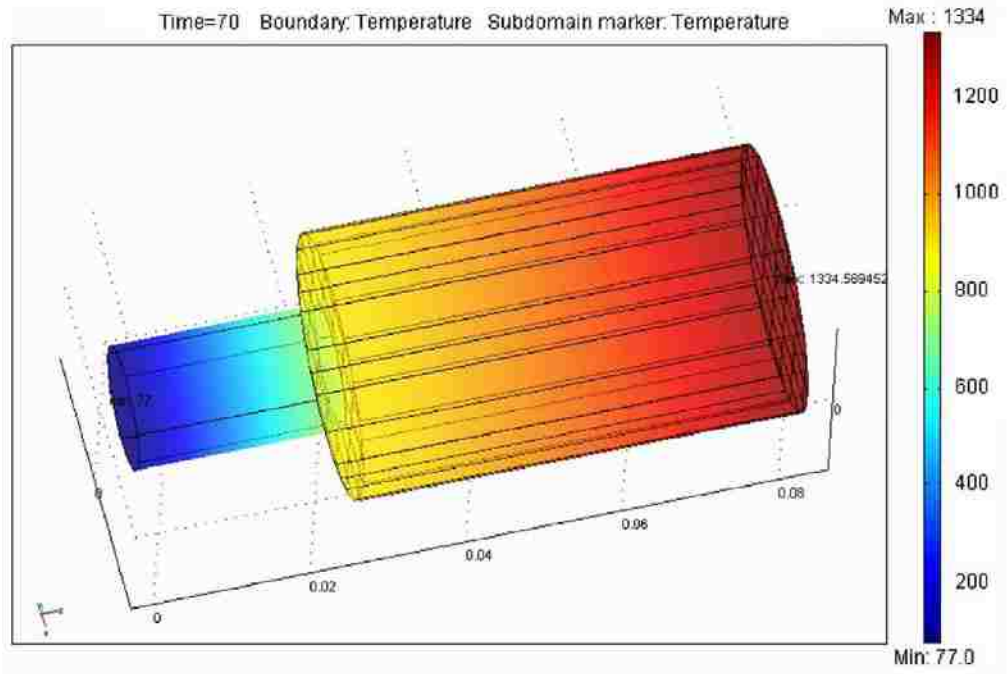

Fig. 8. Target temperature distributions at 70 s, target at −60 kVp with 3 A beam current.

does not provide sufficient operation time. Fig. 8 shows the temperature distribution for the 3 A, −60 kVp in 70 s operation.

In order to provide better thermal management, invaded target configuration was investigated, in which liquid nitrogen is introduced into the target body and closer to the target front. Fig. 9 shows the invaded target temperature distribution for 3 A, −60 kVp in 15 s operation.

Simulation results of the invaded target configuration at 3 A beam current show that the maximum target surface temperature reaches 325 K in 10 s, and remains unchanged

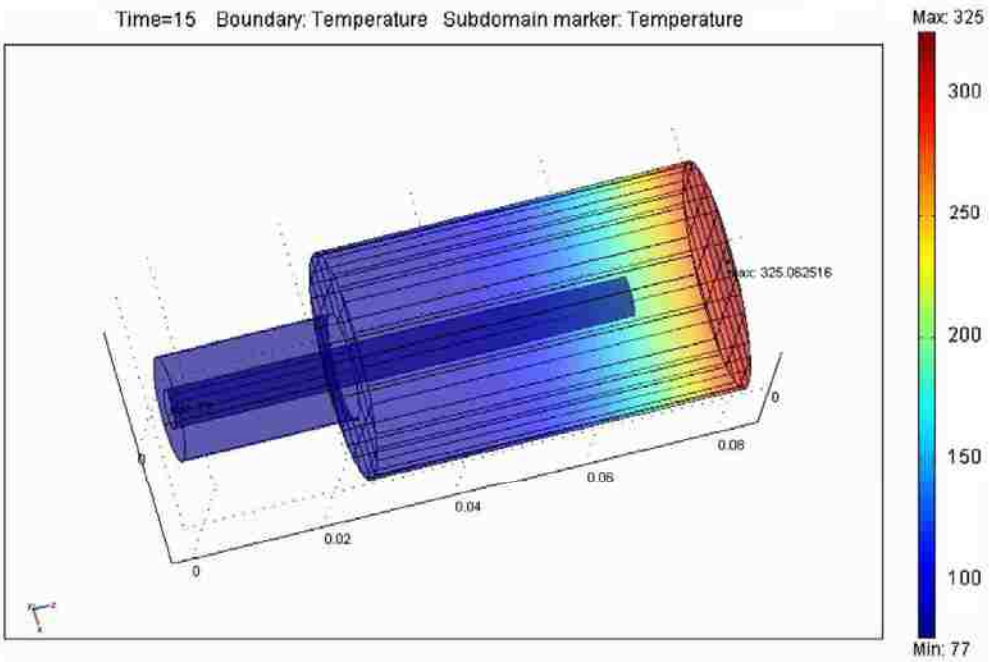

Fig. 9. Target temperature distributions at 15 s, target invaded by liquid nitrogen, at −60 kVp with 3 A beam current.

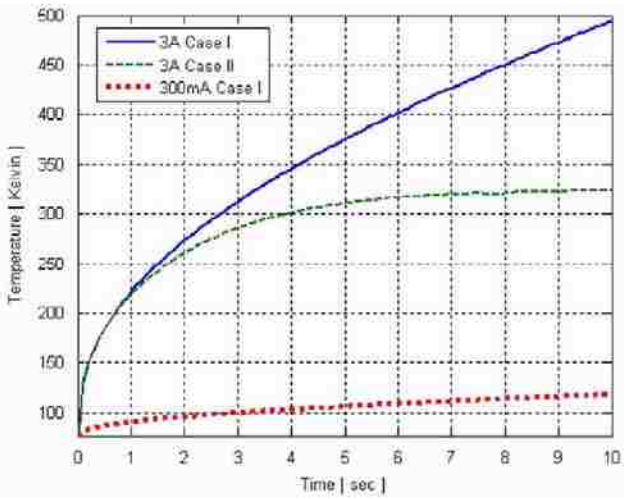

Fig. 10. Maximum target surface temperatures up to 10 s for −60 kVp at 300 mA and 3 A beam currents with contacting cold finger (Case I), and 3 A with liquid nitrogen invaded target (Case II).

thereafter. Fig. 10 shows the maximum target surface temperature as a function of time for 10 s (for the details of initial temperature rise) for 300 mA and 3 A (contacted target, Case I); and for 3 A beam current (invaded target, Case II), while Fig. 11 shows the temperature for both cases up to 100 s.

5.3. Output X-ray flux

The MCNP simulation results are shown in Fig. 12 for aluminum and beryllium, for window thicknesses of 0.01 and 0.05 mm. The normalized characteristic $K_{\alpha 1}$, $K_{\alpha 2}$ and $K_{\beta 1}$ X-ray intensities (particles/mm^2 per total number of

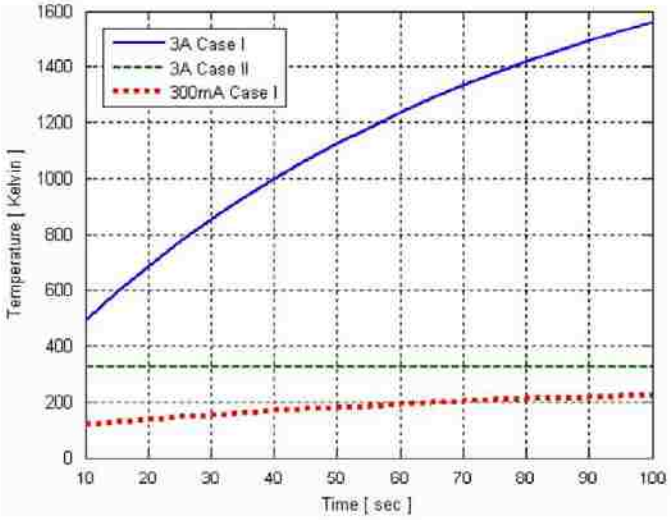

Fig. 11. Maximum target surface temperatures up to 100 s for −60 kVp at 300 mA and 3 A beam currents with contacting cold finger (Case I), and 3 A with liquid nitrogen invaded target (Case II).

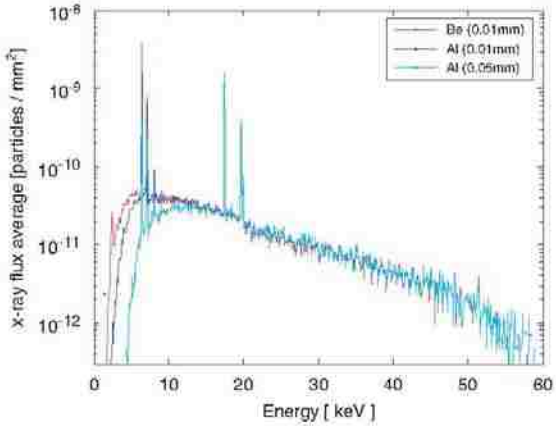

Fig. 12. X-ray spectra with Be and Al window, −60 kVp acceleration.

source particles) are shown in Table 3 for each window thickness. For a given beam current, multiplying the normalized intensity by the total number of the electrons hitting the target (source particles) yields the X-ray intensity for this specific beam current. Aluminum window results show increased intensity with decreased window thickness, while there is no significant change for beryllium windows. However, aluminum windows are more efficient at removing lower energy Bremsstrahlung, which only contributes to the radiation dose. This means that achieving higher X-ray intensity using aluminum windows would require a very thin window, which imposes structural difficulty for a large window under high vacuum. For beryllium, it appears that the window thickness is not a factor and a thicker window might be used. This may be helpful in the engineering design of the window with stronger structure integrity.

The normalized X-ray intensities are obtained from the probability calculated by MCNP multiplied by the total number of electrons per second to obtain the photon flux ($ph/mm^2/s$) for the line of interest that corresponds to the beam current. For a beam current of 3 A, the $K_{\alpha 1}$ X-ray flux for 0.01 mm aluminum window is 2.92×10^{10} $ph/mm^2/s$. For a 0.1 mm beryllium window the computed flux is 2.96×10^{10} $ph/mm^2/s$. Although such window thickness appears to be thin, however techniques of sputter deposition of such thickness are achievable on vacuum glass viewing ports. These X-ray fluxes are less than the synchrotron radiation flux, $\sim 10^{12}$ $ph/mm^2/s$, implying that for a scaled up device area magnification would be necessary to achieve higher flux. The model used in this study is for the molybdenum target area of 6.157 cm^2 and beam current of 3 A. Scaled up device with target surface area of 100 cm^2 provides a factor of 16.242 area magnification. Thus, an overall increase in photon flux would be a factor of 16.242 greater and a flux of 4.808×10^{11} $ph/mm^2/s$ could be achieved, which is comparable to a synchrotron flux of $\sim 10^{12}$ $ph/mm^2/s$.

6. Conclusions

Computational studies of a prototype concentric filament area X-ray source with a tilted stationary target made of molybdenum layer sintered on copper have shown the capability to produce target flux compatible to that of a synchrotron source target flux.

Electron trajectories and their distribution on the target were computed for two different configurations. The backing plate at −60 kVp and the filament biased by

Table 3
MCNP results with Al and Be window

Material	Thickness (mm)	$K_{\alpha 1}$ (particles/mm^2)	$K_{\alpha 2}$ (particles/mm^2)	$K_{\beta 1}$ (particles/mm^2)
Al	0.01	1.56E−09	8.27E−10	3.99E−10
	0.05	1.49E−09	7.83E−10	3.87E−10
	0.1	1.39E−09	7.32E−10	3.66E−10
Be	0.01	1.58E−09	8.35E−10	4.03E−10
	0.05	1.58E−09	8.34E−10	4.03E−10
	0.1	1.58E−09	8.34E−10	4.02E−10

−12 Vp produces a uniform distribution, however, there was a loss of electron population and many electrons miss the target as a result of the diverging electric field. With both the filament and backing plate at −60 kVp the electrons are better focused on the target, which results in less background radiation. Thermal management was investigated with four beam currents, 3, 30, 300 mA, and 3 A. The maximum target surface temperature using a contact liquid nitrogen cold finger with a 3 A beam current exceeded the melting point of copper (1357 K) in 70 s. Using invaded target configuration at 3 A beam current, with liquid nitrogen circulating inside the target, showed that the maximum target surface temperature reaches 325 K in 10 s, and remains unchanged thereafter. The characteristic X-rays $K_{\alpha 1}$, $K_{\alpha 2}$ and $K_{\beta 1}$ of molybdenum target have been investigated for aluminum and beryllium window materials. Simulation results have shown that reduction of the Bremsstrahlung is better with aluminum window over beryllium. The $K_{\alpha 1}$ X-ray flux for a beam current of 3 A with 0.01 mm aluminum window is 2.92×10^{10} ph/mm^2/s, which is two orders of magnitude less than synchrotron source, however, area magnification to 100 cm^2 for a scaled up industrial system could provide the target flux required for DEI applications. An industrial scale device operating at 3 A beam current and a molybdenum target area of 100 cm^2 provides a target flux of 4.808×10^{11} ph/mm^2/s, which is compatible to a synchrotron source target flux. The use of a beryllium window would allow for higher flux at lower beam currents, with the advantage of having a thicker window over a thin aluminum one to sustain high vacuum requirements, however, plasma sputter deposition techniques could be used to deposit thin layer of beryllium on high vacuum viewing windows.

References

[1] F. Shtern, Radiology 183 (1992) 629.
[2] D. Chapman, W. Thomlinson, F. Arfelli, et al., Rev. Sci. Instrum. 67 (9) (1996) CD-ROM.
[3] D. Chapman, W. Thomlinson, R.E. Johnston, et al., Phys. Med. Biol. 42 (1997) 2015.
[4] E.D. Pisano, R.E. Johnston, D. Chapman, J. Geradts, M.V. Iacocca, C.A. Livasy, D.B. Washburn, D.E. Sayers, Z. Zhong, M.Z. Kiss, W.C. Thomlinson, Radiology 414 (3) (2000) 895.
[5] Z. Zhong, W. Thomlinson, D. Chapman, D. Sayers, Nucl. Instr. and Meth. A 447 (2000) 556.
[6] J.D. Budai, W. Yang, N. Tamura, J.-S. Chung, J.Z. Tischler, B.C. Larson, G.E. Ice, C. Park, D.P. Norton, Nat. Mater. 2 (487) (2003).
[7] A.G. MacPhee, M.W. Tate, C.F. Powell, Y. Yue, M.J. Renzi, A. Ercan, S. Narayanan, E. Fontes, J. Walther, J. Schaller, S.M. Gruner, J. Wang, Science 295 (1261) (2002).
[8] E. Abbramyan, Industrial Electron Accelerators and Applications, Hemisphere Publishing Corp., New York, 1988.
[9] J.T. Bushberg, et al., The Essential Physics of Medical Imaging, second ed., Lippincott Williams & Wilkins, Baltimore, MD, 2002.
[10] C.H. Kim, A study of an areas X-ray source for diffraction enhanced imaging for clinical and industrial application, M.S. Thesis, NC State University, August 2004.
[11] D. Chapman, Private Communication, 2001, 2002.
[12] E. Pisano, E. Johnson, D. Chapman, Z. Zhong, D. Sayers, K. Verghese, J.M. Doster, M.A. Bourham, M. Yaffee, Clinical diffraction enhanced mammography unit, NCSU and UNC-CH Invention Disclosure, NCSU File Number 01-59, July 2000.
[13] D.A. Dahl, Idaho National Laboratory, SIMION 3D version 7.0 User's Manual, 2000.
[14] J.A. Halbleib, The Integrated TIGER System in Monte Carlo Transport of Electrons and Photons, Plenum Press, New York, 1988.
[15] J.A. Halbleib, et al., The integrated TIGER series of Coupled Electron/Photon Monte Carlo Transport Codes, Sandia National Lab., Albuquerque, NM, SAND91-1634, 1991.
[16] MCNP—A General Monte Carlo N-Particle Transport Code—Version 5, ORNL/RSICC, April 2003.
[17] CRC Handbook of Chemistry and Physics, 84th ed., CRC Press LLC, 2003–2004.

Chapter 3 Diffraction Enhanced Imaging simulation based on the area x-ray generator

Abstract

A synchrotron-based Diffraction Enhanced Imaging system is not a feasible for clinical applications due to the size of the synchrotron source and the cost associated with operation and maintenance. The proposed area x-ray generator to develop a compact size synchrotron-compatible system, as proposed by North Carolina State University research group in collaboration with University of North Carolina Chapel Hill Radiology group and other, represents a system that can be accommodated in major clinical facilities. In the previous chapter, Chapter 2, on the study of the area x-ray generator it has been shown that generating the $K_{\alpha 1}$ x-ray flux can be comparable to a synchrotron source. In this chapter, Chapter 3, the study investigates imaging using the area x-ray source to produce DEI images through simulation techniques. A MATLAB protocol was developed for 0.8cm×0.8cm field of view, which includes characteristics of an actual focal area, a monochromator, a designed phantom, an analyzer crystal, and an image plate. The major effect of the area x-ray generator in obtaining DEI images originates from the distribution of the electrons on the target. In the current simulation, DEI images are obtained from two different forms of electron distributions, one is for fixed distribution to both lower and higher side images, and the other is used for opposite distributions. The DEI absorption images have strong dependence on the distribution of the electrons, and the refraction image “at the fixed electron distribution” has a blurred edge but more uniform profile through the field of view.

1 Introduction

As it has been previously shown, Diffraction Enhanced Imaging (DEI) has a strong possibility to be employed in the medical field for soft tissue imaging, especially mammography [1-2]. A synchrotron based DEI system has shown high contrast images, however, it is not feasible at the clinical level, and hence the area x-ray generator at high electron beam current is proposed [3]. The computational study, as shown in Chapter 2, has showed that the area beam x-ray generator can provide good features suitable for a DEI system. It has an advantage of reducing the scanning time with the full field of view. However, it also has a disadvantage in the non-uniformity of x-rays due to hot spots from electron distribution on the target. This chapter focuses on studying the effects of non-uniformity on the final DEI images.

2 General considerations

2.1 DEI theory

In 1998, Dean Chapman et al have introduced a new radiography method, called Diffraction Enhanced Imaging, DEI [1]. It is based on the rejection of the scattered x-ray by diffracting x-ray using a Si[333] crystal to act as an analyzer,. Scattered x-rays are considered noise and produce blurring in conventional radiography. The main function of the analyzer crystal is to diffract a selected x-ray beam to the detector. The ratio of the crystal reflectivity, known as the rocking curve, highly depends on the crystal structure. Si[333] crystal has a narrow rocking curve of few microradians at 18 keV, as shown in Figure 3.1, and the reflectivity has its maximum at the exact Bragg condition (zero microradians) and decreases to zero at about ± 4 microradians. For the DEI simulation setup, the analyzer crystal provides

imaging from both the lower and higher sides of the rocking curve, representing the FWHM of the rocking curve, and the obtained two images are used in the DEI algorithm.

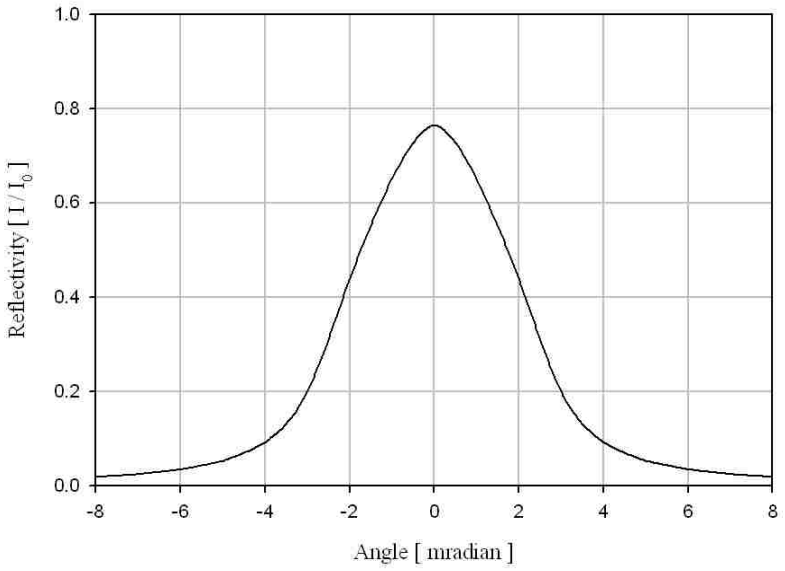

Figure 3 . 1 The Rocking curve of Si[333] with 18 keV x-ray

The intensity of x-ray after the analyzer crystal for any side of the rocking curve can be expressed by the Equation 3.1.

$$I_i = I_R R\left(\theta_0 + \Delta\theta_z\right) \tag{3.1}$$

where I_R is the incoming attenuated intensity to the analyzer crystal, $R(\theta_0+\Delta\theta_Z)$ is the reflectivity at the angle $\theta_0+\Delta\theta_Z$, with θ_0 representing the tuned angle for the FWHM of rocking curve and the $\Delta\theta_Z$ is the small refraction angle by the object. This reflectivity term is expanded in a Taylor's series, and hence the higher (I_H) and lower (I_L) side intensities on the detector can then be expressed by Equations 3.2 and 3.3.

$$I_H = I_R\left(R\left(\theta_H\right) + \frac{dR(\theta_H)}{d\theta}\Delta\theta_Z\right) \tag{3.2}$$

$$I_L = I_R\left(R(\theta_L) + \frac{dR(\theta_L)}{d\theta}\Delta\theta_Z \right) \tag{3.3}$$

These equations can be rearranged for the I_R and $\Delta\theta_Z$. This DEI algorithm applies for the raw image data through pixel-by-pixel. And, the final expression for the DEI image is composed of the refraction angle image $\Delta\theta_z$, and the apparent absorption image I_R as shown in Equations 3.4 and 3.5, respectively

$$\Delta\theta_Z = \frac{I_H R(\theta_L) - I_L R(\theta_H)}{I_L\left(\frac{dR(\theta_H)}{d\theta}\right) - I_H\left(\frac{dR(\theta_L)}{d\theta}\right)} \tag{3.4}$$

$$I_R = \frac{I_L\left(\frac{dR(\theta_H)}{d\theta}\right) - I_H\left(\frac{dR(\theta_L)}{d\theta}\right)}{R(\theta_L)\left(\frac{dR(\theta_H)}{d\theta}\right) - R(\theta_H)\left(\frac{dR(\theta_L)}{d\theta}\right)} \tag{3.5}$$

2.2 Area x-ray beam generator

A DEI system must have a strongly collimated x-ray beam and high photon flux, thus the current DEI experiments are successfully performed using the synchrotron source at the National Synchrotron Light Source (NSLS) of Brookhaven National Laboratory (BNL) for lower energy range (less than 30keV), and the Advanced Photon Source (APS) at Argonne National Laboratory for higher energy range (up to 60keV). These two DEI facilities successfully performed DEI imaging experiments, thus confirming the feasibility of DEI as a new modality [4]. To move from a National Laboratory experimental setup to a clinically-approved system, which can be installed in major medical facilities, a compact size area x-ray generator compatible to synchrotron source is required to be developed. An area beam x-ray generator is a feasible source that can achieve a photon flux comparable to a synchrotron

source [3]. In this research, a conceptual area beam x-ray generator is considered that generates electrons from three concentric filaments in a filament cup. The filament cup can either be biased or float, which alters the formation and distribution of the electrons. High beam current is required for such an x-ray source and thermal management of the x-ray target is a necessity at high beam current of 300mA and 3A; cryogenic active cooling of target may be employed.

2.2.1 Concept

The area x-ray beam from the generator could be quasi-collimated after exiting the x-ray window. The double crystal monochromator works as a filter of the direction and energy. Some of the generated x-ray meets the Bragg condition as they go through the monochromator, and the other x-rays which do not meet the Bragg condition will be extinct or absorbed by the crystal. Therefore, the output x-ray from the monochromator will be in the same direction and at same energy. In case of a conventional x-ray tube, the distribution of the output x-ray is depending on an actual focal area on the target surface. Most conventional x-ray tubes have small focal area on the target, about 3 mm^2 for most commercial x-ray tubes [5], and thus they generate collimated and mono-energetic beam only within the actual focal area which is less then 3 mm^2.

The x-rays from the synchrotron source NSLS of Brookhaven National Laboratory (BNL) for current DEI experiments is covering 80 mm wide and 1mm in height at the location of the object [2]. This synchrotron beam is well collimated and has a flux of 10^7 $ph/mm^2/sec$ at 18keV. Because of the narrow imaging beam, it is required to scan line by line through the vertical direction. A conceptual Figure of narrow beam diffraction on the crystal

is shown in Figure 3.2. For example, to scan 150 mm^2 image it needs 3000 scans for a 50 micro pixel detector plate. The maximum scan time for the synchrotron-based DEI experiment is about 200 sec., which is much less than the scan time of up to 10,000 sec if using a conventional x-ray tube [6] due to the small focal area and the low x-ray intensity.

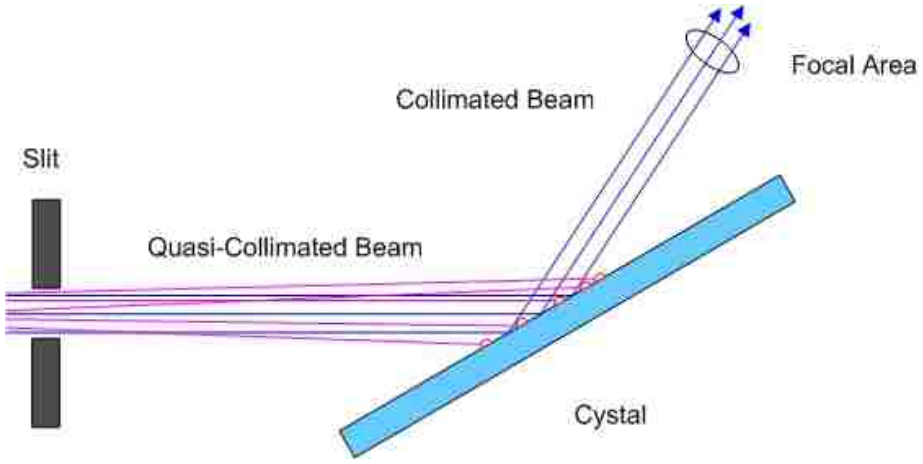

Figure 3 . 2 Narrow beam diffraction concept

The proposed concept of an area x-ray generator, for an up-scaled version for commercial use, has an actual focal area of about 100 cm^2 on the target, while the North Carolina State University prototype lab-version source is 6.157 cm^2. For a large crystal, the diffraction will occurred through the entire crystal surface and the beam is much wider. It is possible for the prototype lab-version to have about 2.4 cm^2 of actual focal area on the detector plate when the target angle is 22.5 degree. A conceptual drawing of the large focal area diffraction is illustrated in Figure 3.3. Therefore, the wide beam x-ray generator will eliminate line by line scanning process, and hence the total scanning time can greatly be reduced for feasibility as an attractive DEI application in the medical field. A long scanning time is not desirable and creates motion artifacts, which is more important for medical applications, specifically for mammography. Additionally, most mammography systems

require object compression during the entire scanning time. But, the DEI can provide more comfortable examination through eliminating the compression procedure. Such advantages are achievable with the area x-ray source. However, non-uniformity of the electron distribution on the actual focal area may be problematic. The x-ray flux profile on the image plate depends on the electron distribution on the target and the non-uniformity of the electron distribution could generate spotted images.

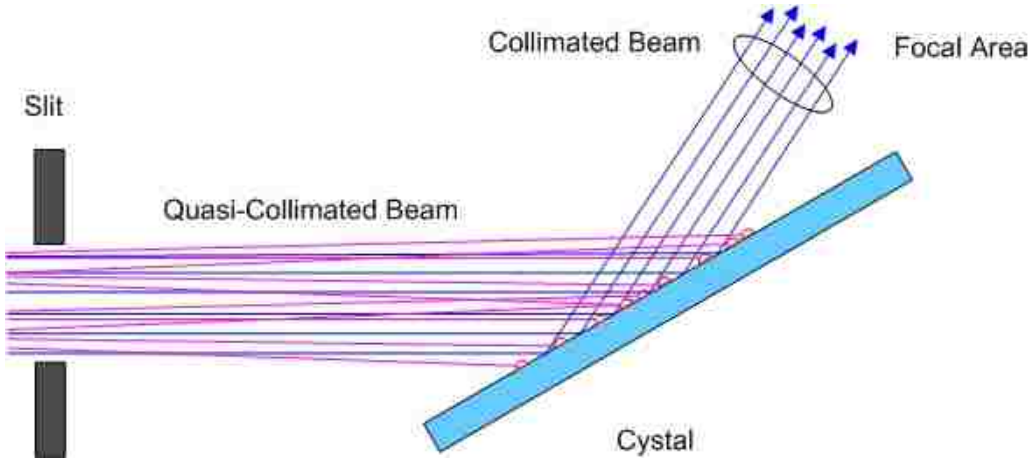

Figure 3 . 3 Wide beam diffraction concept

3 Method

In this study, computational simulations were performed to obtain DEI images and analyze the artifacts from the wide beam x-ray generator. The final DEI images were obtained by using 2-dimensional convolution with each imaging component. Equation 3.6 shows the simulation kernel.

$$I_{image}^{side} = (I_{source} \otimes\otimes I_{rad} R(\theta_{side} + \Delta\theta_z)) \otimes\otimes PSF + Noise \qquad (3.6)$$

where, I_{source} is the monochromatized x-ray intensity and it has the electron distribution

based on the actual focal area, $R(\theta_{side}+\Delta\theta_z)$ represents the reflectivity function of the analyzer crystal, *PSF* is the point spread function representing the response of the image plate. Quantum noise is also added to the final images. The lower and higher side images are obtained using the above kernel, and the refraction and absorption images are generated by applying the DEI algorithm to each pixel, on a pixel by pixel regime.

3.1 Monochromatized beam

Typical x-ray tube has a continuous energy spectrum, which is shown with Bremsstrahlung and some characteristic x-ray peaks. As previously indicated the target is oxygen free copper with a layer of molybdenum; here the focus is on the $K_{\alpha 1}$ x-ray flux form the molybdenum target. It is computationally assumed that the monochromator is tuned to the $K_{\alpha 1}$ x-ray energy, which met the Bragg condition, and located at the maximum flux position next to the x-ray window. The monochromatized x-ray beam is shown as a source function in the simulation kernel, where the source function represents the x-ray intensity response of the monochromator from a point electron source. Therefore, two features should be considered, the maximum intensity from a single electron hitting on the target and the electron distributions on the target. The energy spectrum at the maximum flux position from a point electron source is shown in Figure 3.4. The target angle was set to the 22.5 degree, which corresponds to the maximum angle for the prototype lab-version device. Only the x-rays of the $K_{\alpha 1}$ energy will be allowed and all others will be eliminated by the crystal. Therefore, the source function, which represents the monochromatized beam through the imaging area, can be obtained by convolution of the reflectivity of the crystals [7]. The electron distribution on the target surface for a non-floating filament assembly is shown in Figure 3.5.

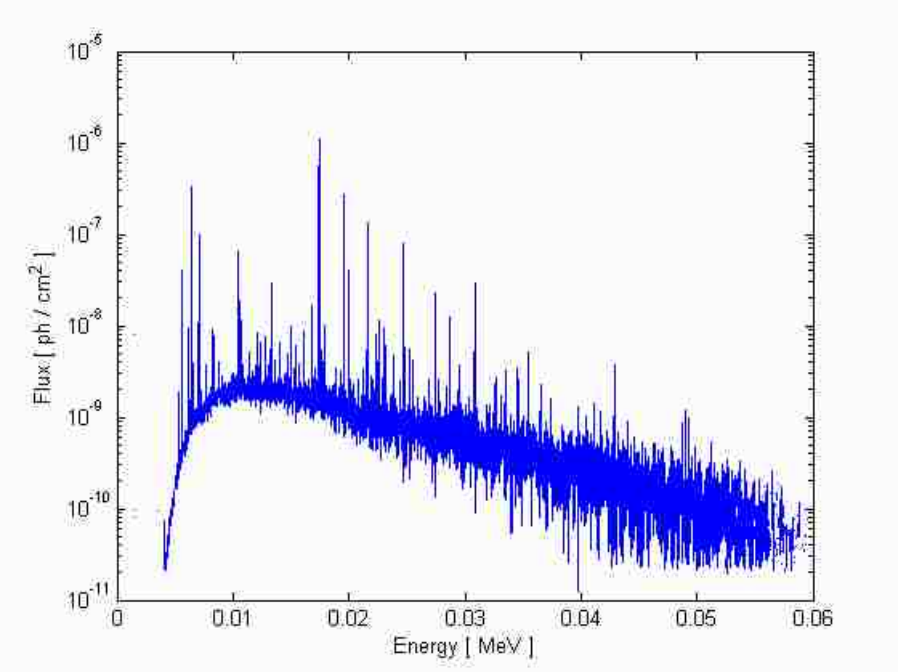

Figure 3 . 4 X-ray distribution from the point electron source at the maximum flux position

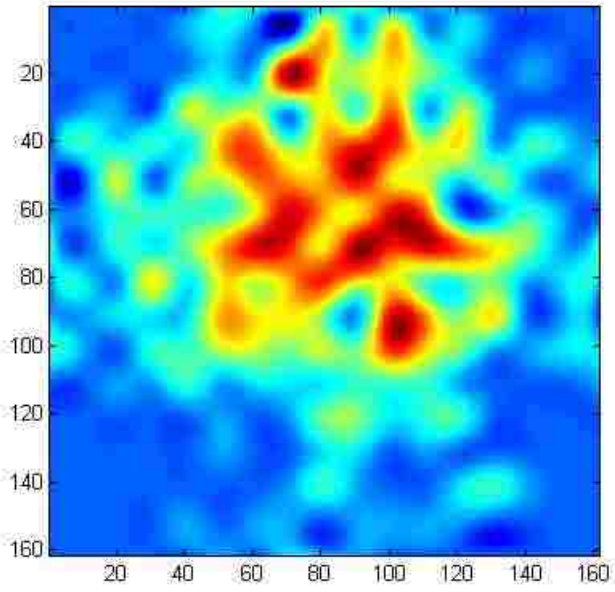

Figure 3 . 5 Electron distributions on the target surface

3.2 X-ray optics on the phantom

3.2.1 Phantom design

An appropriate mammogram phantom is computationally designed to simulate DEI images based on the use of the prototype lab-version area x-ray source. Breast cancer is classified by the location of cancerous tissue and tumor size. There are two type of pre-cancer, the Ductal Carcinoma In Situ (DCIS) and the Lobular Carcinoma In Situ (LCIS). Such pre-cancers are likely to develop to invasive cancer. The physiological characteristic of these pre-cancers show some calcification on their respective regions. Breast cancer studies show that a large calcification is not usually associated with cancer, but small calcifications, microcalcification, are related to cancer [8]. Based on the interest in soft tissues and micro-calcification, the phantom in this simulation was chosen to contain two materials, nylon and aluminum oxide. Table 1 shows the properties of these materials, also air properties are added.

Table 3 . 1 Material properties of phantom material

Object	Air	Tissue	Calcification
Equivalent material	Air	Nylon fiber Type 6/10	Al_2O_3
μ at 18 keV [cm^{-1}]	1.47×10^{-3}	0.616	11.77
Density [g/cm^3]	1.29×10^{-3}	1.14	3.69
Refractive Index $n=1-\delta$	≈ 1	$\delta = 8.56\times10^{-7}$	$\delta = 2.46\times10^{-7}$

The shape of the phantom is basically cylindrical, one large cylinder of nylon containing a small rod of aluminum oxide, as shown in Figure 3.6. The image simulation code, built within MATLAB, allows the user to change the diameter and location of the aluminum oxide rod inside the nylon cylinder.

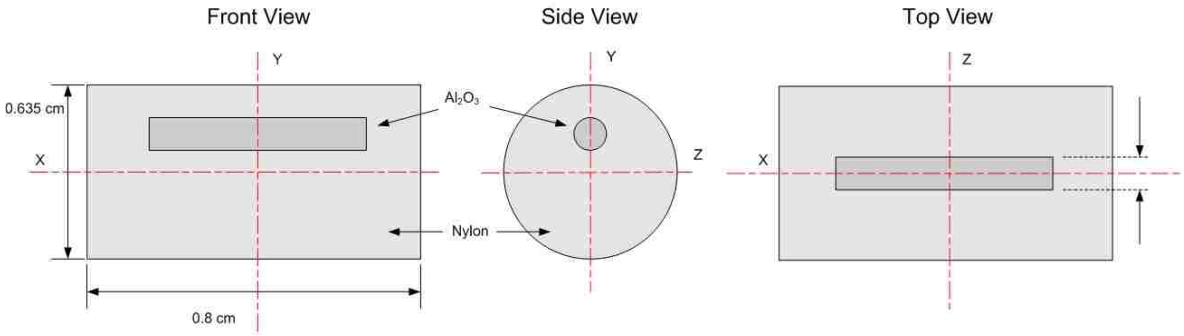

Figure 3 . 6 Phantom design

3.2.2 X-ray path through the object

The image simulation code is designed to calculate the attenuation and refraction with the simulation phantom. The x-ray path way has been divided into two regions by the geometry features, a single cylinder region and a dual cylinder region. The single cylinder region is shown in Figure 3.7, and is similar to the single cylinder phantom previously considered by Kiss [9]. As seen from Figure 3.7, the single cylinder is a solid nylon surrounded by air, the incident x-ray falls on the cylinder in the location y_1 by an angle θ_1^i , traverses the cylinder and exiting with a refractive angle. The incident angle of the x-ray beam on the cylinder can be calculated from Equation 3.7.

$$\theta_1^i = \sin^{-1}\left(\frac{y_1}{r_1}\right) \tag{3.7}$$

When the beam penetrates the object it undergoes two refractions and the refraction angle can be calculated from the Snell's law of refraction. The final refection angle is approximately twice of the single refraction angle and is expressed by Equation 3.8.

$$\Delta\theta_Z \approx 2\tan(\theta_1^i)\left[\frac{n_{air}}{n_{tiss}} - 1\right] \tag{3.8}$$

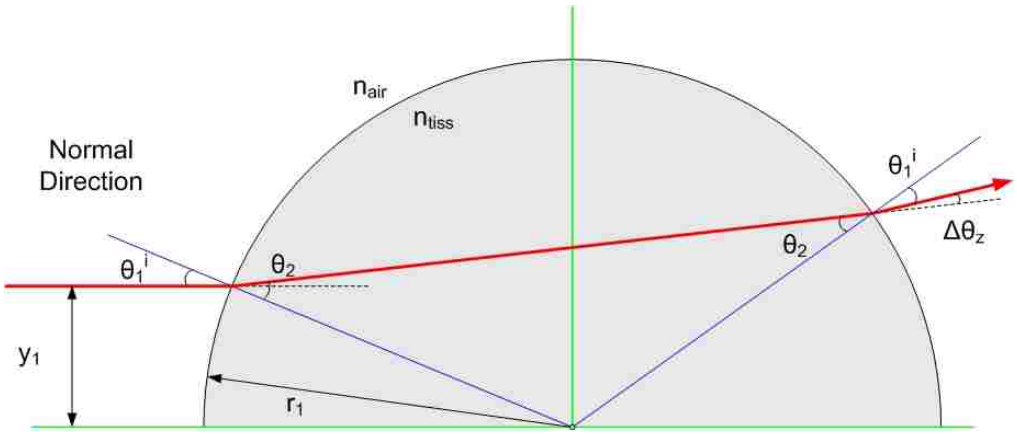

Figure 3 . 7 X-ray pathway inside of single cylinder object

In the dual cylinder configuration the x-ray beam refracts first in the nylon cylinder then incident on the calcification rod. In this case, the same equation for first region is applicable and is used for the incident and refraction angles. The incident angle onto the calcification rod is determined by the first refraction angle and the location of calcification rod. Consequently, the pathway of the incident x-ray on the dual configuration is subject to multiple refractions in the nylon cylinder and the calcification rod. Figure 3.8 shows the x-ray pathway in the dual cylinder configuration, which complicates the calculation of x-ray pathway and refraction angle.

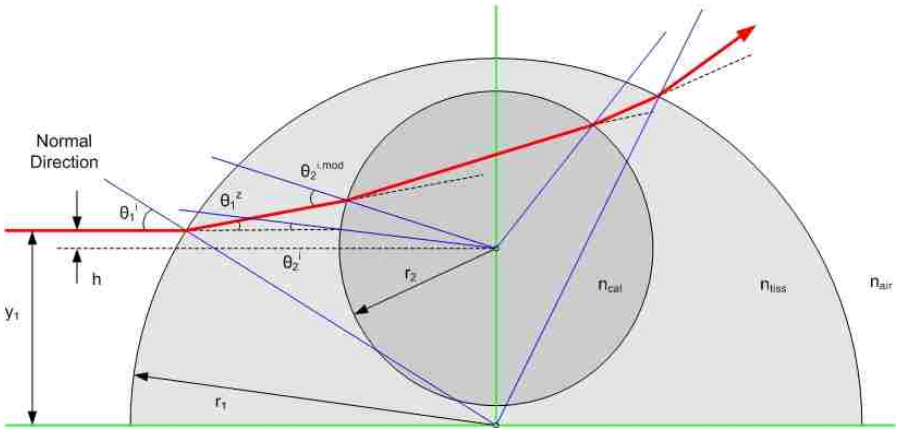

Figure 3 . 8 X-ray pathway inside of dual cylinder object

Two assumptions were applied to these calculations. The first assumption is that the x-ray travels into the objects in a straight line, which means that the refraction angle doesn't affect x-ray attenuation through the objects. The maximum refraction angle by the first cylinder, the nylon, is 1.0×10^{-5} radian, which is very small compared to the object's diameter 0.635 cm. This assumption simplifies the calculation of x-ray travel length through the entire objects. The second assumption is that the second incident angle $\theta_2^{i.mod}$ does not change by the first refraction angle θ_1^z. Therefore, modified second incident angle is defined as the summation of the first refraction angle and the incident angle, which is calculated with x-ray location, h. The definition of angles is given in Equations 3.9 and 3.10. The final refraction angle in this region is same as per the single cylinder case, which follows Equation 3.8 again with the second incident angle $\theta_2^{i.mod}$. These two assumptions minimized calculation complexity, also reduced errors on the second assumption by the first assumption.

$$\theta_2^{i.modfied} = \theta_2^i + \theta_1^z \tag{3.9}$$

$$\theta_i^2 = \sin^{-1}\left(\frac{h}{r_2}\right) \tag{3.10}$$

3.3 Image plate

The DEI algorithm is applied after obtaining the raw image, which contains characteristics of an image plate, Point Spread Function (PSF) and Dynamic Range (DR). Possible x-ray detectors for DEI were compared By Kiss et al [10]. The Fuji BAS2500 Image Plate Reader shows the largest dynamic range and active area among CCD devices, Mar USA and MicroPhotonics XQUIS 1000. In his study, the Fuji BAS2500 Line Spread Function(LSF) for the vertical and horizontal direction was measured instead of Point Spread

Function. The Fuji BAS 2500 Image plate data are shown in Table 3.2, in which it is obvious that the vertical and horizontal FWHM have similar value and therefore the Point Spread Function can be considered as one of them. A Fuji image plate reads at latitude (L) of 5 and sensitivity(S) of 4000 with 16 bit gray level. The reader converted raw x-ray intensity I_{raw} to output data I_{in} withas shown in Equation 3.11. The Dynamic Range is defined as a ratio between maximum intensity on the detector and the background noise, which is 1.4×10^5 for the Fuji BAS2500 image plate. The detailed data were shown in Table 3.2

$$I_{in} = \frac{4000}{S} 10^{L(I_{raw}/G - 0.5)} \tag{3.11}$$

Table 3 . 2 Fuji BAS 2500 Image plate data [10]

	Fuji BAS 2500
Pixel size	50 μm
Pixel format	4000 × 5000 pixels
Image area	200 × 250 mm^2
Gray level	16-bit
Readout time	5 min
Horizontal FWHM	145±1μm (2.9±0.1 pixels)
Vertical FWHM	138±1μm (2.8±0.1 pixels)
Saturation level	1.4×10^4 photon / pixel
Noise level	0.101 photon / pixel
Dynamic range	1.4×10^5
Latitude	5
Sensitivity	4000

4 Image simulation results

The image simulations were performed for the case of a non-floating filament

assembly, 30 mA electron beam current, Si[333] double crystal monochromator and analyzer, and a Fuji BAS2500 Image Plate. The full field of view of the simulation is 0.8 cm × 0.8 cm. The diameter of the nylon cylinder is 0.635cm, and the aluminum oxide rod is 0.05 cm diameter. After obtained the raw images on the image plate, the DEI algorithm was applied to pixel by pixel for DEI refraction and absorption images. The simulations are also tested for different electron distributions on the x-ray target. Figure 3.9 shows the electron distribution used for simulation, in which distribution (a) is a projection view of the actual focal area as obtained from SIMION simulation of electron trajectories, and distribution (b) which is a flipped over from the original distribution. The DEI images, lower side, higher side, absorption and refraction images are shown in Figure 3.10. The images are truly affected by the electron distribution, but the effect is reduced for the refraction image because it only represents the refraction angle difference between the raw lower side and higher side images. Image blurring is observed at the edge of the nylon cylinder, where partial image blurring occurs at places of low electron density on the target.

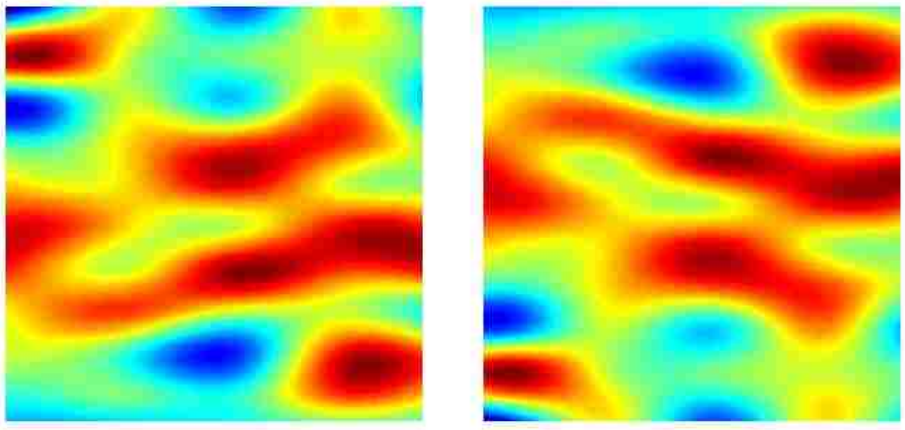

Figure 3 . 9 Electron distribution on the actual focal area. (a) original (b) flipped over

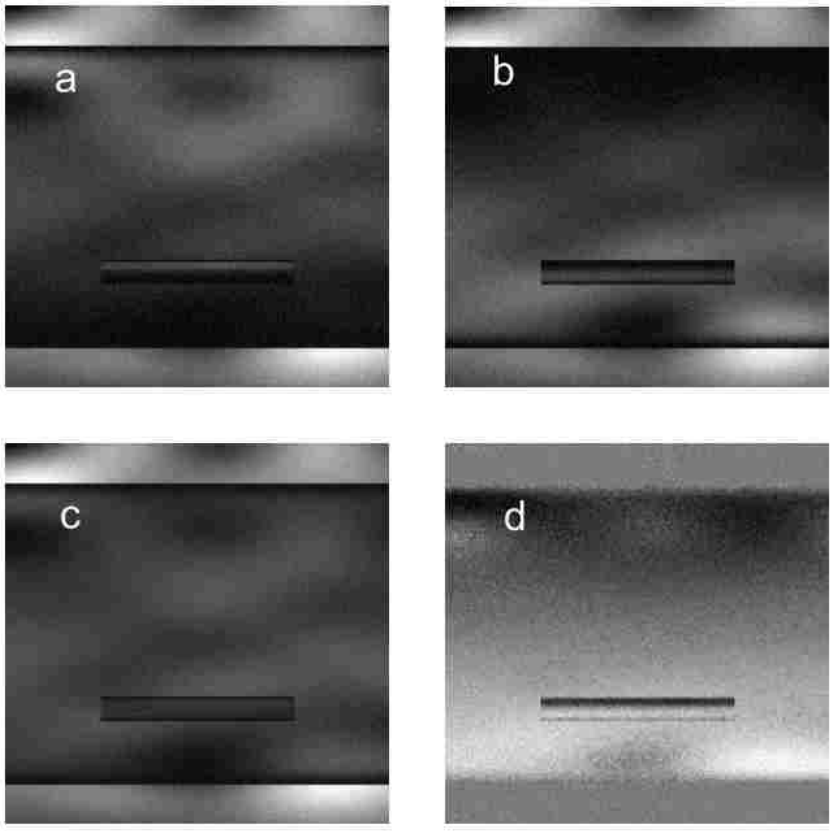

Figure 3 . 10 Images based on the fixed electron distribution, a. scaled higher side image, b. scaled lower side image, c. absorption image, d. refraction image

The second simulation was performed with an idea of varying the electron distribution at time of each side scan. In this case it was assumed that the distribution of the electrons is a 'flipped over' for the entire image surface. Image simulation was obtained for the higher side of the rocking curve using the original electron distribution with same data of the first simulation. The lower side image was generated by the electron distribution (b), the flipped over distribution. Figure 3.11 shows the obtained images. In this simulation, the absorption image contained the bright regions from the both side images. The refraction image had less blurring on the edge of the Nylon. Also, the region of aluminum oxide rod showed typical DEI refraction image characteristic, dark on the higher and bright on lower. But, the effects

from the electron distribution increased and showed highly spotted refraction image.

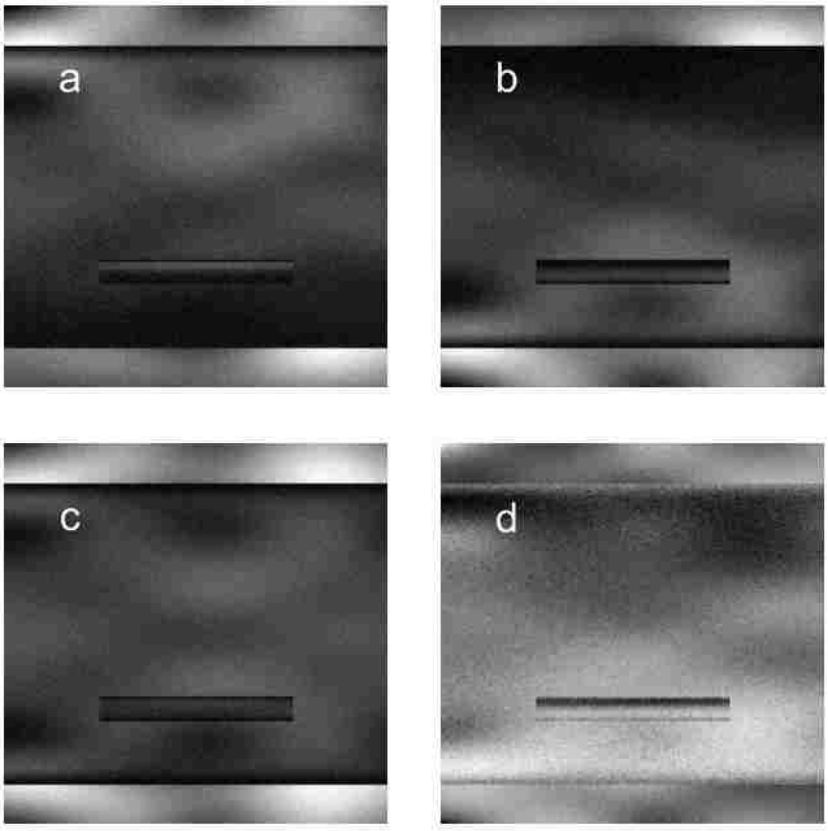

Figure 3 . 11 Images based on the different electron distribution, a. scaled higher side image, b. scaled lower side image, c. absorption image, d. refraction image

5 Conclusion

The area beam x-ray generator is adequate for DEI application and can obtain images in a reasonable time. However, electron distribution on the actual focal area produces non-uniformity on the whole DEI images. In this research, MATLAB protocols 'codes' were written to simulate effects of the actual focal area distribution on the final DEI images. The developed protocols include the Si[333] crystal monochromator response, x-ray optics on the designed phantom and the response of the Fuji BAS2500 image plate. Two DEI image sets

were obtained using two different electron distributions on the target. The first image set was obtained from applying same electron distribution to the lower and higher side images. The DEI absorption images contained similar intensity distribution through the whole images, which is a natural outcome based on the expression of the absorption image. In case of the refraction image, some regions showed similar intensity shapes with blurring at the edge of nylon cylinder. However, the image is more uniform compared to the absorption image. The second simulation was performed with different electron distributions, one for the higher side image and one for the lower side image. The DEI absorption image shows some overlap image, with increased non-uniformity on the refraction image but decreased edge blurring. Refraction images in both cases remained at good resolution for the aluminum oxide region, which simulates the calcification inside the nylon cylinder.

References

[1] Chapman D, Thomlinson W, Johnston RE, et al. Diffraction enhanced x-ray imaging, Phys. Med. Bio. 42: 2015-2025, 1997.

[2] Pisano ED, Johnston RE, Chapman D, Geradts J, Iacocca MV, Livasy CA, Washburn DB, Sayers DE, Zhong Z, Kiss MZ, Thomlinson WC. Human Breast Cancer Specimens: Diffraction-enhanced Imaging with Histologic Correlation - Improved Conspicuity of Lesion Detail Compared with Digital Radiography, Radiology 414(3), 895-901, 2000.

[3] Chang H. Kim, Mohamed A. Bourham, J. Michael Doster, A wide beam x-ray source suitable for diffraction enhanced imaging application, Nuclear Instrument and Method in Physics Research A 566: 713-721 ,2006.

[4] Zhong Z., Thomlinson W., Chapman D., Sayers D. Implementation of Diffraction

Enhanced Imaging at the NSLS and APS, Nuclear Instrument and Method in Physics Research A 447: 556-568, 2000.

[5] Jerrold T. Bushberg et al, The Essential Physics of Medical Imaging, 2nded., Lippincott Williams & Wilkins (2002), Baltimore Maryland

[6] Wang, Xiaoqin, Line x-ray source for diffraction enhanced imaging in clinical and industrial application, Appendix D, Ph.D Dissertation, NC State University, 2006.

[7] Miklos Z. Kiss, Application of diffraction enhanced imaging for obtaining improved contrast of calcifications in breast tissue, Appendix A. Ph.D Dissertation, NC State University, 2002.

[8] www.breastcancer.org

[9] Kiss MZ, Sayers DE, Zhong Z, Measurement of imaging contrast using diffraction enhanced imaging, Phys. Med. Bio. 48: 325-340, 2003.

[10] Kiss MZ, Sayers DE, Zhong Z, Comparison of X-ray detectors for a diffraction enhanced imaging, Nuclear Instrument and Method in Physics Research A 491: 280-290, 2002.

Chapter 4 Focal area optimization of the wide beam x-ray source

Abstract

Previous studies of wide beam x-ray sources have shown compact systems can be engineered that are adequate for Diffraction Enhanced Imaging applications with sufficiently high photon flux and production of strongly collimated x-rays. The x-ray distribution on the imaging surface depends on the focal area distribution, which is based on the characteristics of the monochromator's response. Therefore, the focal area distribution impacts the image quality and the local heat loading, with the latter determining the limits on system operating time. This study seeks to optimize focal area uniformity by independently powering the three concentric filaments in the proof of principle design. Electron distributions and their trajectories are simulated. The focusing cup voltage is set to -60kVp. Each filament has a separate voltage to independently generate electrons at different rates. Evaluation of uniformity is determined by the standard deviation and peak-to-average ratio. The independent voltage biasing of the filaments has shown that improved distributions can be obtained when the outer filament is at -60kVp, the middle one is at -48kVp and the inner filament is at -40kVp.

1 Introduction

The study of Diffraction Enhanced Imaging has shown higher contrast images for materials with lower attenuation coefficient, which provides for a more favorable x-ray modality for soft tissue imaging, specifically in clinical applications for mammography [1-4]. Experiments performed with a synchrotron radiation source at high photon flux and strongly

collimated x-ray beam have shown high contrast images as compared to conventional radiography. [5]. All conventional x-ray tubes generate low-flux beams that diverge at large angles, and are thus less collimated, which makes conventional sources inadequate for DEI applications. Development of an area x-ray beam has shown the potential to provide synchrotron-comparable photon fluxes from sources of sufficiently small size to fit in a compact integrated x-ray DEI system, suitable for installation in major medical facilities and hospitals [6].

Previous studies of the wide beam x-ray source focused primarily on the production of the required x-ray flux from concentric filament designs with all filaments at the same potential leading to non uniformities in the electron distributions on the target [7]. In the image simulation study, non uniformities in the electron distribution resulted in some loss of phantom information due to saturation of the image plate [8]. Additionally, hot spots or localized high heat flux, can result in target melting, damage and deterioration, especially for the target's thin molybdenum layer. In this study, the electron distribution on the target surface is improved by independently biasing the filaments at different voltages.

2 General considerations

In general, the x-ray tube cathode consists of a filament or a dual filament inside a focusing cup, which provides electron control and focus prior to acceleration towards the target. The filaments and focusing cup are usually at negative potential and the target is at positive potential or ground, thus providing the necessary electric field for electron acceleration and steering towards the target [9]. In conventional x-ray tubes, the electron trajectories are directed to a tiny spot on the target. This small focal spot reduces image

blurring. In the DEI system the double crystal monochromator serves to select a specific x-ray energy range and collimates the beam. X-rays from the source diverge to the x-ray window, where most of the x-rays do not meet the Bragg condition of the crystal and are eliminated. If the monochromator and analyzer crystals are stable and tuned to the exact Bragg angle, then the electron distribution on the target will be the main artifact for DEI imaging. It can be assumed that the actual focal area in the DEI setup represents the x-ray flux on the imaging surface.

Electron trajectories are determined by the filament's electric potential and the biasing potential on the filament cup [9]. Biasing the filament cup is more effective in producing a small actual focal area, but a larger focal area is required for the proposed wide beam x-ray source. The filament assembly for this specific design is composed of three concentric filaments housed inside the focusing cup. The spatial distribution of the electrons generated by thermionic emission from the filaments depends on the location of the filaments and the amount of electric power into each filament. If all filaments are powered at same level, then the electron generation would be non-uniform with a peak in the center. The resulting electron density at the target would be higher at the center resulting in the development of hot spots. An un-biased filament cup in a floating configuration produces a more divergent shape and therefore can be helpful in producing a more uniform electron distribution on the target and minimize generation of hot spots.

3 Simulation of electron trajectories

3.1 Design parts

The wide beam x-ray source is composed of three concentric circular filaments in a

filament cup, and an actively-cooled oxygen-free copper target with a molybdenum layer [7]. Figure 4.1 illustrates the three filament assembly, the focusing cup and the supporting structure. The radius of the focusing cup is 2.15 cm and the radius of each filament is shown in Table 4.1.

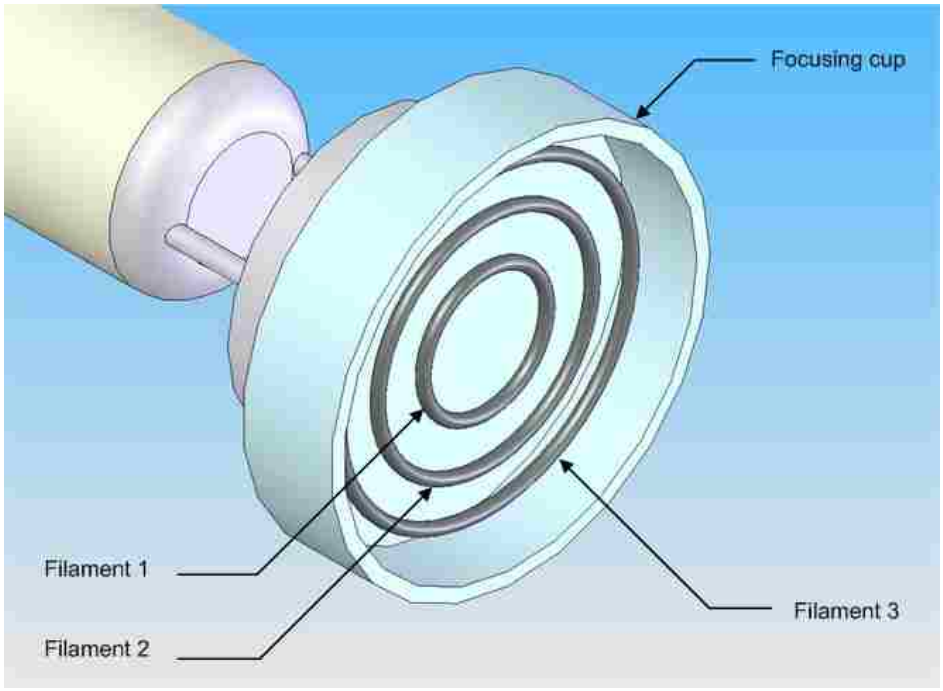

Figure 4 . 1 Filaments assembly design

Table 4 . 1 Filaments data

Filament	location	Radius
# 1	inner	0.701 cm
# 2	middle	1.215 cm
# 3	outer	1.658 cm

3.2 Simulation options

Simulation of electron trajectories and their distribution was performed with the

SIMION 3D code [10]. The filament assembly can either be at common voltage with common current to all filaments or each filament be powered independently. In previous simulations, all filaments were interconnected and thus the voltage to all filaments was equal in both floating and non-floating configurations [7]. In this chapter, an investigation of independent filament biasing is conducted in order to improve the uniformity of the electron distribution on the target. Figure 4.2 illustrates the filaments when all are floating (Fig. 4.2a) and when all are connected and non-floating (Fig. 4.2b). The focusing cup is at -60kVp for all simulations. The first simulation considers the effects arising from the voltage changes on each filament. All filaments are assumed to be floating. One filament voltage would be reduced from -60kVp to -40kVp in 10kVp steps. This provides four simulation tests, for each voltage change on a single filament there will be simultaneous change for the two other filaments. Based on the first simulation results, the second simulation would be performed on a narrower voltage change of 2kVp at the determined voltage range.

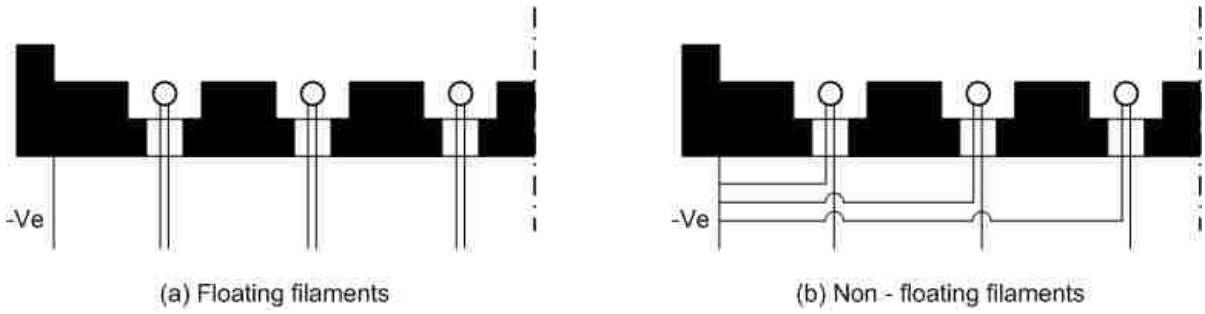

Figure 4 . 2 Schematic drawing of the floating and non floating filaments' connection

Electron distribution on the target surface is recorded and plotted by 15 x 15 arrays, where the size of the single array is ~ 0.23 cm. The entire array represents the whole 9.186cm^2 surface area of the proof-of-principle target. Two parameters are used to compare

the uniformity of the electron distribution on the surface, the standard deviation and the peak-to-average ratio. Additionally, the electron utilization, which is the ratio between the number of generated electrons from the filaments and the number of landed electrons on the target, is also used in the comparison. The definitions of standard deviation and peak-to-average ratio are given in Equations 4.1 and 4.2, respectively

$$STD = \left(\frac{1}{n-1} \sum_{i=1}^{n} \left(x_i - \overline{x} \right)^2 \right)^{1/2} \tag{4.1}$$

$$\Omega = \frac{x_{max}}{\overline{x}} \tag{4.2}$$

where, $\overline{x} = \frac{1}{n} \sum_{i=1}^{n} x_i \quad , n = 225$

The simulation results for this case of independent power to each filament are compared to the previous simulation results of the biased filaments at -60kVp [7]. The obtained simulation results can also be compared with a reasonable assumption that the electrons landed uniformly on the target surface, this means that under such assumption the standard deviation and the peak-to-average ratio would be zero and unity, respectively. Therefore, a lower value of the standard deviation and a close to unity peak-to-average ratio would be preferred. The average number of electrons on each array, under such assumption, would be about 5.17 at a uniform distribution.

4 Results and discussion

The results of the first simulations are shown in Table 4.2 for all four simulation options. For option 1, the outer and middle filaments are kept at -60kVp and the inner

filament was varied from -60kVp to -30kVp in 10kVp stepping down regime. One distinctive feature on the results is that the outer filament is better to be at the same voltage of the focusing cup. The outer filament not only generates electrons but also has an additional feature in electron repulsion and thus reducing escape of electrons. Figure 4.3 shows electron trajectories for two cases, option 1 with the inner filament at -40kVp (Figure 4.3 a: outer at -60kVp, middle at -60kVp and inner at -40kVp), and option 3 with the outer filament at -40kVp (Figure 4.3 b: outer at -40kVp, middle at -60kVp and inner at -60kVp). The electron loss is higher when the outer filament is at a potential less than the focusing cup, as seen from Figure 4.3b, and thus maintaining the outer filament at the focusing cup potential reduces electron loss.

The first simulation results showed that the outer filaments should be at the filament cup potential at -60kVp. The case of -60kVp for the middle filament and -40kVp on the inner filament is showing the lowest standard deviation and high utilization of 98%.

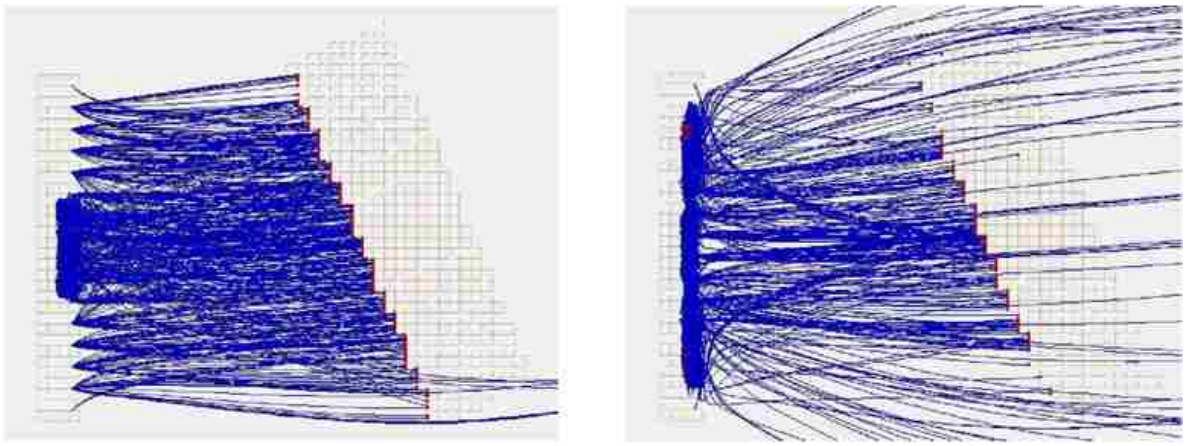

(a) Outer : -60 kVp, Middle : -60 kVp, Inner : -40 kVp (b) Outer : -40 kVp, Middle : -60 kVp, Inner : -60 kVp

Figure 4 . 3 Electron trajectories from SIMION simulation

Table 4 . 2 First simulation results

Option	Outer	Middle	Inner	Utilization	STD	Average	Ω
1	-60		-60	0.97	4.23	4.36	7.03
			-50	0.98	4.85	4.41	6.75
			-40	0.98	3.53	4.37	4.95
			-30	0.94	3.91	4.25	5.09
2	-60	-60	-60	0.97	4.23	4.36	7.03
		-50		0.94	8.17	4.18	22.20
		-40		0.73	5.07	3.30	14.75
		-30		0.70	3.83	3.20	9.86
3	-60	-60		0.97	4.23	4.36	7.03
	-50			0.76	5.25	3.41	13.23
	-40			0.49	5.16	2.23	25.88
4	-60	-60	-60	0.97	4.23	4.36	7.03
		-50	-50	1.00	7.62	4.49	8.42
		-40	-40	0.87	4.42	3.94	7.10
		-30	-30	0.71	3.65	3.26	5.81

The second simulation applies more detailed voltage changes for this option by maintaining the outer and middle filaments at -60kVp and varying the inner filament's voltage between -30 to -50kVp on 2kVp steps. Figure 4.4 shows the change in the standard deviation and the peak-to-average ratio over the entire range of change of the inner filament's voltage. The standard deviation is the lowest at -40kVp and rises if the potential would be increased or decreased, and the peak-to-average ratio is also at its lowest in this configuration. The second simulation confirms the results of the primary one indicating that the best combination is for the outer and middle filaments at -60kVp and the inner one at -40kVp.

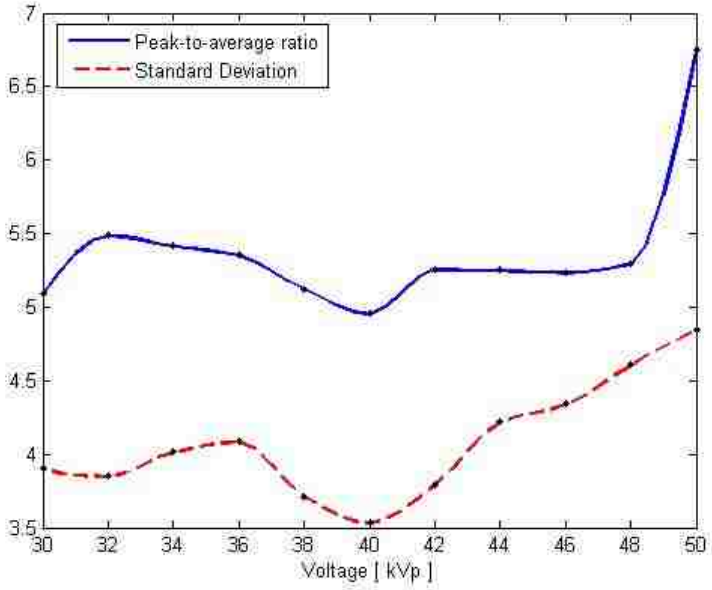

Figure 4 . 4 Standard deviation and Peak-to-average ratio VS Inner filament voltage change (outer and middle : -60kVp)

The third simulation focused on option 2 in which the outer and inner filaments are both at -60kVp, and varying the middle filament voltage between -60 to -30kVp on 10kVp steps. In this option it is also shown that the least standard deviation is when the middle filament is at the lowest voltage. A simulation was performed with varying middle filament voltage on 2kVp increments while maintaining the outer and inner filaments at -60kVp and -40kVp, respectively. Figure 4.5 shows that the key parameters, standard deviation and peak-to-average ratio, increase and peaking at -54kVp, and decrease for potentials above or below the -54kVp. Table 4.3 shows the change in the parameters for all changes in the middle filament potential for this case, in which it is obvious that the lowest standard deviation (3.93) and peak-to-average ratio (3.64) is when the middle filament is at -48kVp and the corresponding utilization is 100% thus indicating no electron loss.

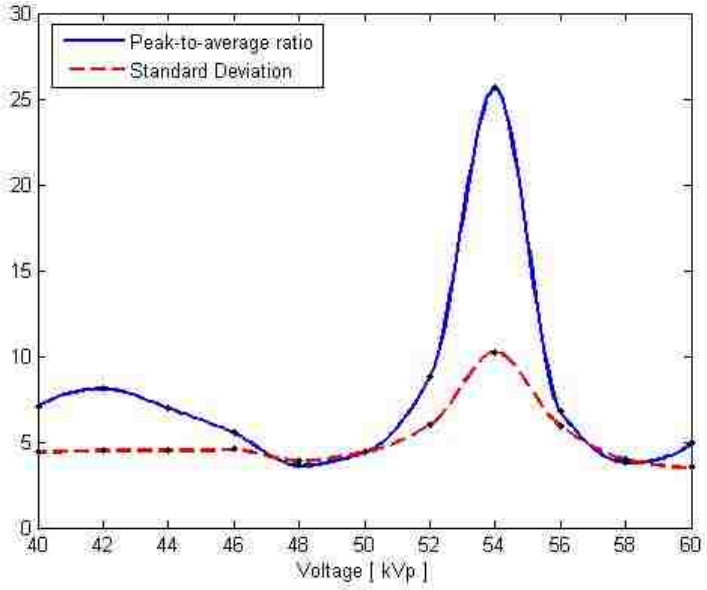

Figure 4 . 5 Standard deviation and Peak-to-average ratio VS Middle filament voltage change (outer : -60kVp, inner : -40kVp)

Table 4 . 3 Third simulation results

Outer	Middle	Inner	Utilization	STD	Average	Ω
	60		0.98	3.53	4.84	4.95
	58		0.99	3.99	4.95	3.84
	56		1.00	5.96	4.99	6.82
	54		1.00	10.26	4.99	25.67
	52		1.00	6.01	4.99	8.83
60	50	40	1.00	4.42	4.99	4.41
	48		1.00	3.93	4.95	3.64
	46		0.99	4.56	4.88	5.53
	44		0.95	4.54	4.74	6.97
	42		0.91	4.52	4.43	8.14
	40		0.87	4.42	4.37	7.10

The standard deviation is a little higher than the minimum value obtained in the second

simulation, but this result of the third simulation provides higher utilization and peak-to-average ratio. The electron trajectory and their distribution on the surface of the target are shown in Figures 4.6 and 4.7, respectively. As seen from Figure 4.6, all electrons emanating from the filaments land on the target without any loss. Figure 4.7 (a) shows the best result among the performed simulations. Figure 4.7 (b) shows the electron distribution from the non-floating filaments option. These figures show that the uniformity of electron distribution was improved by the independent powering of each filament.

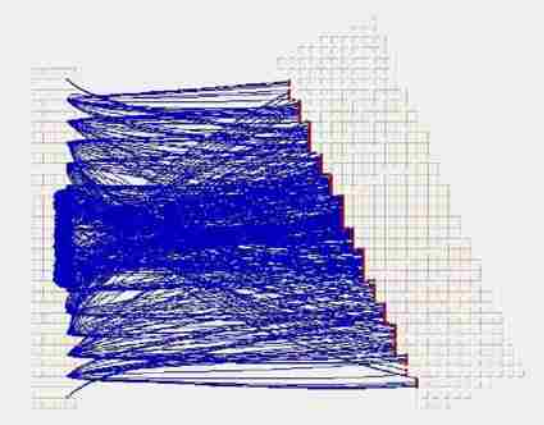

Figure 4 . 6 Electron trajectories from SIMION – Floating filaments option (outer: -60kVp, middle: -48kVp, inner: -40kVp)

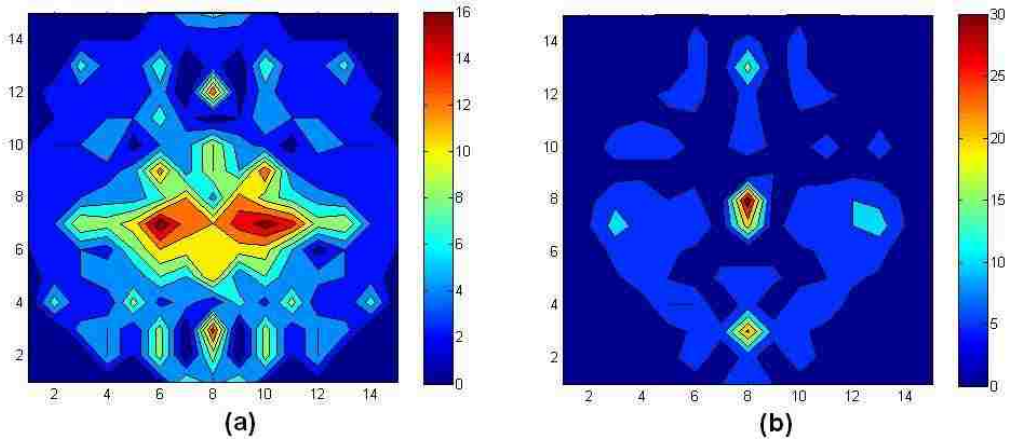

Figure 4 . 7 Electron distribution on the target surface, (a) Floating filaments option (outer: -60kVp, middle: -48kVp, inner: -40kVp), (b) Non-Floating filaments option (outer: -60kVp, middle: -60kVp, inner: -60kVp)

5 Conclusion

A large area, wide beam x-ray source has advantages over conventional x-ray tubes for DEI applications. Electron trajectories in conventional x-ray tubes are focused on a tiny focal spot on the target. For DEI applications that require beam currents of up to 3A, the small focal spots would be at extreme heat loadings. The x-rays will be limited by the electron focal area after passing through the monochromator, and thus the wide beam x-ray source is advantageous in providing less operation time.

In this study, the three concentric filaments assembly was tested via computational simulation and compared to the floating filament concept. The first simulation shows that the outer filament provides repulsion force on the electrons and reduces losses if it would be kept at the same potential of the filament cup at -60kVp, and that a lower voltage on the inner filament helps to disperse electron trajectories to the target. For the quantitative comparison, the standard deviation and the peak-to-average ratio were used as measures of the optimized independent filament performance. The final simulation results showed that the option of having the outer filament at -60kVp, the middle at -48kVp and the inner at -40kVp, results in minimum standard deviation and peak-to-average ratio, and achieved 100% of electron utilization. Therefore, wiring of the filaments in the filament cup should be independent to achieve better utilization on the target and near uniform distribution. Filaments may use the same power supply with potential dividers to provide the required voltage to each filament from one common power supply.

Reference

[1] Shtern F. Digital Mammography and Related Technologies: A Perspective From the National Cancer Institute, Radiology 183:629-630, 1992.

[2] Chapman D, Thomlinson W, Arfelli F, et al. Mammography Imaging Studies using a Laue Analyzer Crystal, Rev. Sci. Instrum. 67(9): CD-ROM, 1996.

[3] Chapman D, Thomlinson W, Johnston RE, et al. Diffraction enhanced x-ray imaging, Phys. Med. Bio. 42: 2015-2025,1997.

[4] Pisano ED, Johnston RE, Chapman D, Geradts J, Iacocca MV, Livasy CA, Washburn DB, Sayers DE, Zhong Z, Kiss MZ, Thomlinson WC. Human Breast Cancer Specimens: Diffraction-enhanced Imaging with Histologic Correlation - Improved Conspicuity of Lesion Detail Compared with Digital Radiography, Radiology 414(3), 895-901, 2000.

[5] Zhong Z., Thomlinson W., Chapman D., Sayers D. Implementation of Diffraction Enhanced Imaging at the NSLS and APS, Nucl. Instrum. Meth., In Phys. Res. A447: 556-568, 2000.

[6] E. Pisano, E. Johnson, D. Chapman , Z. Zhong, D. Sayers, K. Verghese, J.M. Doster, M.A. Bourham and M. Yaffee, “Clinical Diffraction Enhanced Mammography Unit”, NCSU and UNC-CH Invention Disclosure, July 2000, NCSU File Number 01-59.

[7] Chang H. Kim, Mohamed A. Bourham, J.Michael Doster, A wide-beam X-ray source suitable for diffraction enhanced imaging application, Nucl. Instrum. Meth, In Phys. Res. A566:713-721,2006.

[8] Chang H. Kim, Mohamed A. Bourham, “Diffraction Enhanced imaging simulation based on the area x-ray generator”, to be submitted to Phys. Med. Bio. 2007

[9] Jerrold T. Bushberg et al, The Essential Physics of Medical Imaging, 2nd ed., Lippincott

Williams & Wilkins (2002), Baltimore Maryland

[10] D.A. Dahl, Idaho National Laboratory, SIMION 3D version 7.0 User's Manual, 2000.

Chapter 5 Target thermal management simulation using inner jet cooling concept

Abstract

A wide beam area x-ray source has been proposed as a practical replacement for synchrotron sources in clinical DEI applications. The proposed x-ray source can be employed in major medical facilities due to its compact size, reasonable dimensions and power requirements. This source provides a wide x-ray illumination area and has characteristics comparable to synchrotron radiation. Due to the large focal area, a decrease in x-ray flux is expected and thus high electron beam currents of up to 3A are considered. At such high beam currents, the heat loading on the target can be significant and limit the operational time of the target. The anticipated scanning time for a DEI system is a few seconds, and thus target thermal management is essential to ensure target performance without deterioration, melting, cracking or even evaporation. An active cooling system is required for the target block in order to remove the heat and allow for sufficient scanning time. In this study, jet cooling of the target back is investigated for a prototype proof-of-principle target. The prototype target was simulated with the transient k-ε turbulence multiphysics model in ANSYS CFX. The jet nozzle was designed to produce the maximum convective heat transfer coefficient for the range of coolant velocities considered. The simulations were conducted at a heat flux of 1.8×10^{7} W/m^{2}, consistent with values anticipated for a full scale target. The target temperature exceeds the copper melting point in 2 seconds at inlet velocities below 2 m/sec. The results show that a 3.5 m/sec inlet velocity at atmospheric pressure is a lower limit for prevention of target burnout using water as a coolant.

1 Introduction

In the proposed compact wide-beam x-ray source for Diffraction Enhanced Imaging applications, the major requirements are a highly collimated, high intensity photon flux [1-3]. Conventional x-ray tubes can not meet these requirements due to their relatively low x-ray flux and the fan shape of the x-ray beam. To increase x-ray flux to compete with a synchrotron radiation beam, a high electron beam current (up to 3A) is proposed in conjunction with a large x-ray illumination area. Heat removal in a conventional x-ray source is not a critical issue because lower electron beam currents are used and a rotating target allows for spreading the heat flux over a larger area of the target [4]. Conventional x-ray tubes which use stationary targets are passively cooled with air or oil. The wide-beam x-ray source in this study has a stationary target (anode) and hence heat removal at high beam currents is essential. For a device expected to operate at the commercial level, a 3A beam current would be required in order to generate the necessary high x-ray flux. At 60kV acceleration potential, this is a 180kW system that requires special thermal management for target heat removal. The estimated scanning time of a DEI-based wide beam x-ray system is ~20 sec during which time the beam energy will be converted to heat energy on the target [5]. The cooling demands of such a target exceed the heat removal capacity of a passive cooling system and necessitate an active cooling system.

Early research work on the wide beam x-ray system considered cryogenic cooling using liquid nitrogen through a contact or invaded cold finger [1]. This study revealed that heat removal via conduction utilizing liquid nitrogen could not obtain the required operating time before the target reached its melting temperature. In addition, the large thermal gradients and induced stresses in such a system would render it infeasible.

In this study, an inner impinging jet cooling method was employed for active cooling with water at atmospheric pressure and room temperature. The prototype proof-of-principle design was simulated using the ANSYS CFX finite element code.

2 General considerations

Due to the high heat loads, target thermal management is an important issue for the proposed wide beam x-ray system. Impinging jet cooling has been shown as an effective way to remove heat from the heated surface in various devices, and is considered in this study for target cooling [6]. Design of a jet cooling system requires maximizing the convective heat transfer from the target back while satisfying thermal limits associated with maximum target temperatures and critical heat flux. Convective heat transfer can be maximized by optimizing the geometry of the jet nozzle. To maintain target integrity, maximum target temperatures must remain well below the melt temperature. This is dictated by the target materials, geometry and the efficiency of the target cooling system. If the heat flux at the coolant/target interface exceeds the critical point, transition to film boiling can occur degrading heat transfer and potentially leading to target failure [7].

2.1 Convective heat transfer coefficient

Impinging jet cooling is a widely used method for many engineering applications and has been studied as a function of both the fluid characteristics and the shape of the jet [8-11]. Correlations for the convective heat transfer coefficient are a function of the ratio of the exit-to-impingement distance to the jet exit diameter (S/d) and the ratio of the diameter of the impingement surface to the jet exit diameter (D/d) [13]. For $2 \leq S/d \leq 12$, $5 \leq D/d \leq 15$ and

$2000 \leq Re_d \leq 400{,}000$, the convective heat transfer coefficient for a submerged, single jet water nozzle can be expressed in terms of the Nusselt number through the empirical equation.

$$Nu = \frac{d}{D}\frac{\left[2 - 4.4\frac{d}{D}\right]}{\left[1 + 0.2\left(\frac{S}{d} - 6\right)\left(\frac{d}{D}\right)\right]} F\left(Re_d\right) Pr^{0.42} \tag{5.1}$$

where $F(Re_d)$ is a power function of Reynolds number and Pr represents the Prandtl number [6]. The power function, $F(Re_d)$, is shown in Equation 5.2

$$F\left(Re_d\right) = 2Re_d^{0.5}\left[1 + \frac{Re_d^{0.55}}{200}\right]^{0.5} \tag{5.2}$$

The Prandtl number satisfies the general definition of viscous diffusion rate over thermal diffusion rate.

2.2 Critical heat flux

Generally an impinging jet causes a stagnation point on the surface and therefore, the critical heat flux q_{CHF} will occur at the stagnation point. A non-dimensional correlation for the critical heat flux in a simple forced convection boiling system with an impinging jet is shown by Equation 5.3 [14].

$$\frac{q_{CHF}/\left(\rho_v h_{hg}\right)}{u} = 7.45\times10^{-2}\left(\frac{\rho_l}{\rho_v}\right)^{0.725}\left(\frac{\sigma}{\rho_l u^2 D}\right)^{1/3}\left(1 + \varepsilon_{sub}\right) \tag{5.3}$$

Where ρ_v and ρ_l represent vapor and water density, h_{hg} is the latent heat of vaporization, u is the jet velocity, σ is the surface tension of water and ε_{sub} is a correction factor for liquid subcooling, shown in Equation 5.4.

$$\varepsilon_{sub} = 2.7 \times \left(\frac{\rho_l}{\rho_v}\right)^{1/2} \times \left[\frac{Cp\left(T_{sat} - T_l\right)}{h_{fg}}\right]^{2.0} \tag{5.4}$$

3 Nozzle design in the x-ray target

As previously mentioned, the wide beam x-ray target is a cylindrical stationary target made of oxygen-free copper with a thin layer of molybdenum which acts as the x-ray generating material [1]. Figure 5.1 illustrates the target design and its dimensions for the prototype proof-of-principle system fabricated by Brand X-Ray, LLC, Wood Dale, IL, USA. Figure 5.2 shows the initial configuration of the jet nozzle.

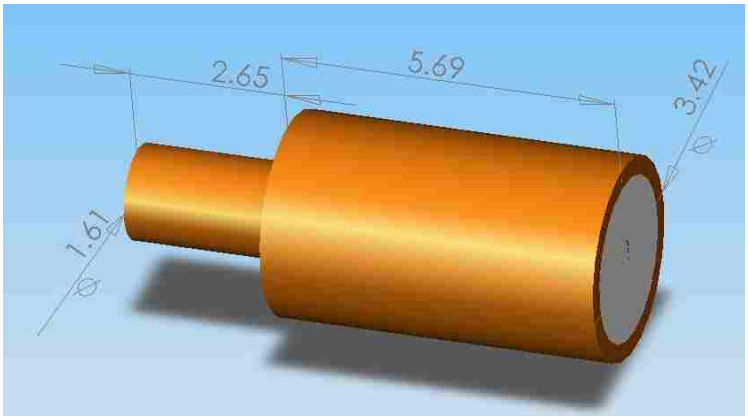

Figure 5 . 1 Wide beam x-ray oxygen free target with layer of molybdenum [1]

The convective heat transfer coefficient can be found from the Martin correlation (Equation 5.1) for a single submerged jet in water [6]. Based on the Reynolds number range for the correlation, the fluid velocity is between 0.2 m/sec and 33 m/sec, which is adequate for the proposed application. In case of 1 m/sec inlet velocity, the Reynolds number is varying from 2366 to 5366 depend on d changes from 2.4 mm to 5.6 mm. The convective heat transfer coefficient as a function of S/d and D/d is shown in Figure 5.3. The convective

heat transfer coefficient increases with the decrease in the S/d ratio. At any given S/d, the heat transfer coefficient also increases with the decrease in the D/d ratio. The diameter of impingement surface D is fixed as the target diameter. As the Martin correlation has lower limit on the D/d ratio of 5, this sets the optimum nozzle diameter, which in turn sets the optimum nozzle to target spacing. The optimized design is shown in Figure 5.4 with dimensions that correspond to a S/d ratio of 1.8 and D/d ratio of 5.15.

Figure 5 . 2 Configuration of the impinging jet nozzle

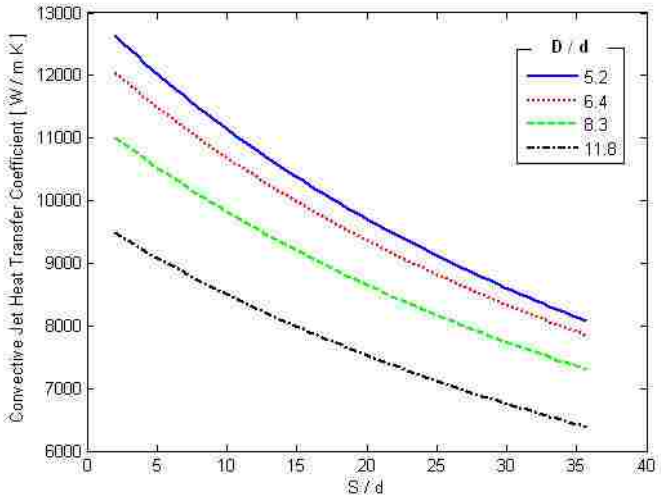

Figure 5 . 3 Convective heat transfer coefficient as a function of S/d for various values of D/d

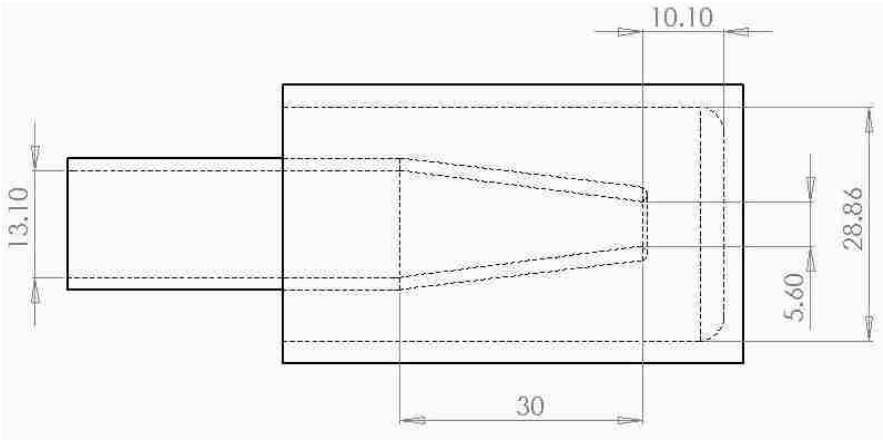

Figure 5 . 4 Optimized jet nozzle design (units: mm)

3.1 Equivalent beam current

The proof of principle target is designed to operate at the same heat flux as the industrial scale target. To provide the necessary photon flux for practical clinical or industrial screening applications has been shown to require power levels of 180 kW on the target for beam currents at 3A and an accelerating potential of –60 kVp. For an industrial scale target area of 100 cm^2, this implies an inward heat flux on the target of 1.8 x 10^7 W/m^2. As the proof of principle target is designed to have a surface area of 10 cm^2, the target heat flux can be obtained using an order of magnitude less beam current of 300 mA.

4. Simulation results and discussion

Simulation of target performance was performed using the finite element code ANSYS CFX. The initial designs for the target, the jet nozzle and the fluid volumes were created with the CAD tool Solidworks. The input mesh file for ANSYS CFX was generated by the meshing tool ICEM CFD. The transient k-ε turbulent flow model was used to model the fluid

behavior. Room temperature water was chosen as the coolant.

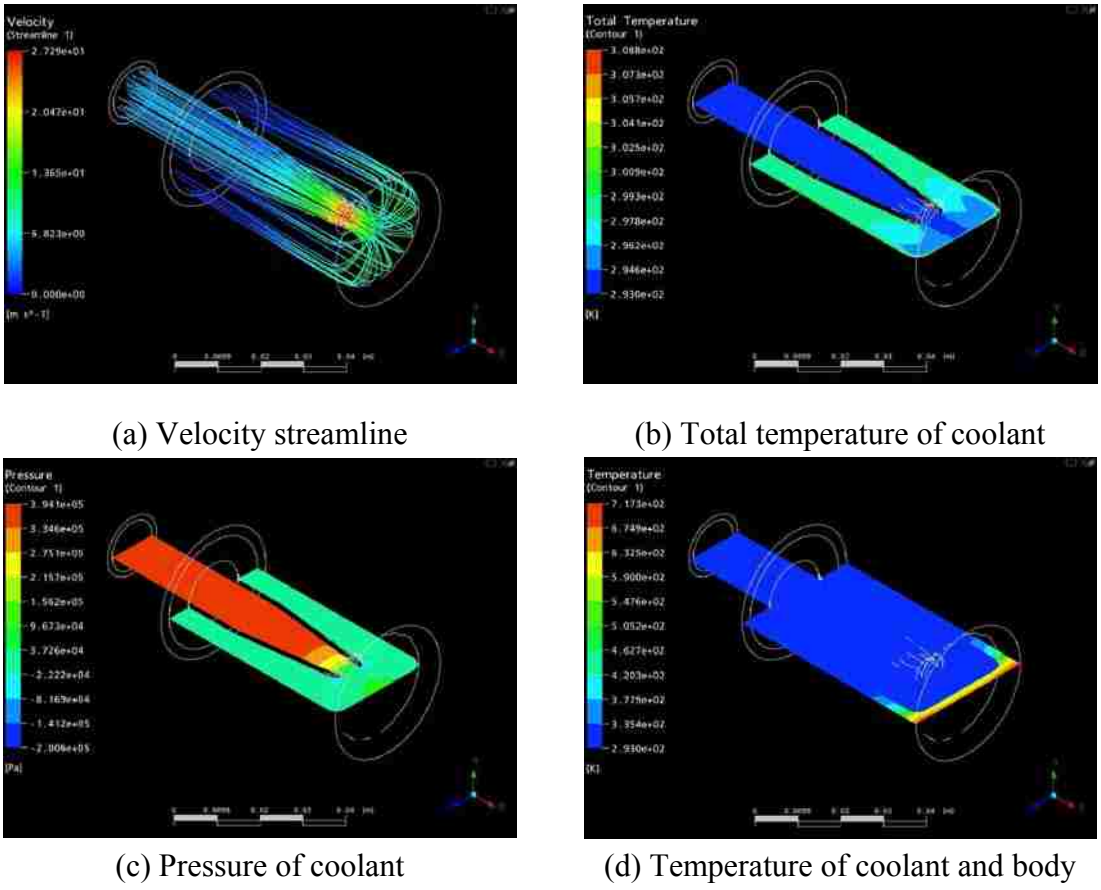

(a) Velocity streamline (b) Total temperature of coolant

(c) Pressure of coolant (d) Temperature of coolant and body

Figure 5 . 5 ANSYS CFX results at 20 sec (inlet velocity : 5m/sec, beam current 300mA)

Room temperature water with a uniform velocity distribution was assumed at the inlet to the back of the nozzle. The target face is subject to a uniform inward heat flux of 1.8×10^7 W/m^2. Otherwise, the target's outer surface is considered thermally insulated, radiative losses are neglected. Solid-to-fluid and fluid-to-solid interface boundary conditions were applied to the target body-coolant and the coolant-jet nozzle in this simulation. It is also assumed that the coolant channel is at atmospheric pressure. Inlet velocities were examined between 1 m/sec and 9 m/sec. Figure 5.5 shows the ANSYS CFX simulation results for an inlet velocity

of 5m/sec at 20 sec, for a 300mA electron beam current.

Figure 5.5 (a) shows the fluid velocity stream lines. The inlet fluid velocity is 5 m/sec and increases up to 27 m/sec at the nozzle exit. Figure 5.5 (b) shows the fluid temperature. The fluid temperature remains constant at the inlet value until impinging upon the target surface. After hitting the target surface, the fluid temperature increases and exits the rear of the target. A single jet nozzle produces a stagnation point at the impinging surface. The stagnation point is shown as bright green in Figure 5.5 (c). The temperature distribution through the target body and the fluid is shown in Figure 5.5 (d). The maximum temperature at the heated surface is 717 K.

The design of the impinging jet cooling system must satisfy two conditions; the maximum target temperature must be below the melting point, and the inward heat flux must be below the critical heat flux. In this target design the target body is made of oxygen free copper with a thin layer of molybdenum serving as the x-ray source. The melting points of molybdenum and copper are 1356^{o}K and 2896^{o}K, respectively and hence the copper melting point is considered as the temperature limit. Figure 5.6 shows the maximum target temperature as a function of time for inlet water velocities of 3, 5 and 7 m/s. It is clear that increasing the coolant velocity decreases the target temperature. For example, increasing the coolant velocity from 3 to 7m/s drops the maximum target temperature from 820^{o}K to 650^{o}K. Figure 5.7 shows the coolant temperature at the stagnation point for the same three inlet velocities. Increasing the coolant inlet velocity also decreases the coolant temperature. For example, increasing the velocity from 3 to 7m/s reduces the maximum coolant temperature from 318^{o}K to 305^{o}K. The critical heat flux depends on the coolant velocity at the nozzle and the temperature at the stagnation point. Figure 5.8 shows the predicted critical heat flux as a

function of the coolant inlet velocity, where it is obvious that the critical heat flux increases with increased velocity.

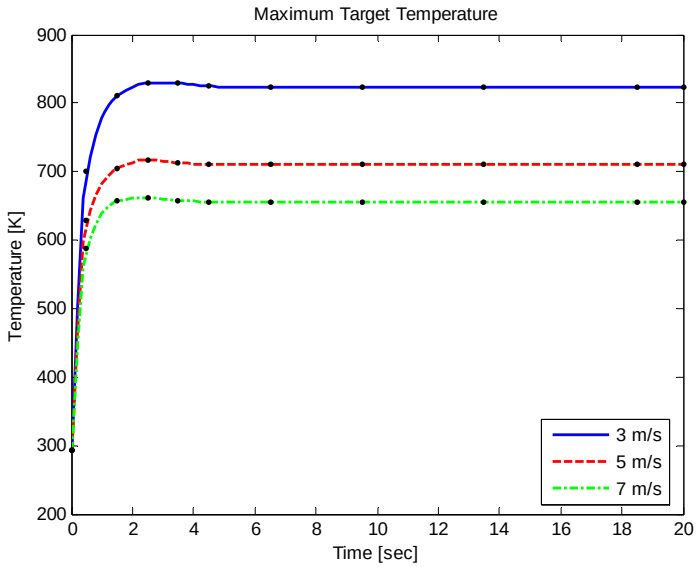

Figure 5 . 6 Maximum target temperature as a function of time for 3 different coolant inlet velocities (300mA beam current)

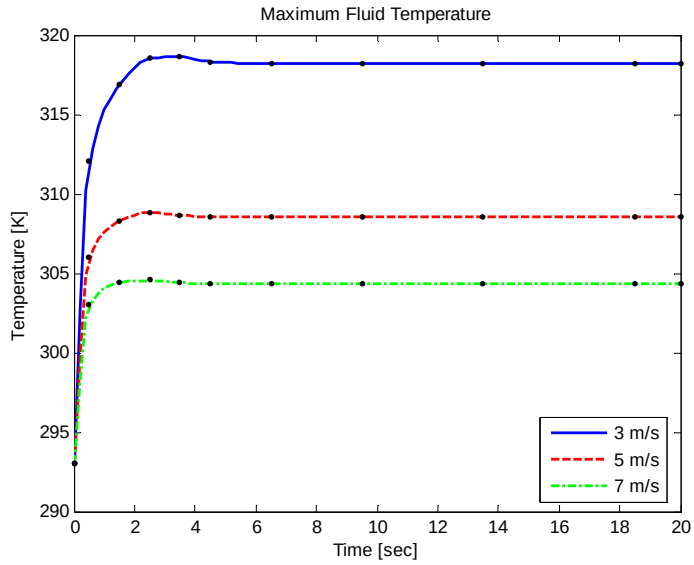

Figure 5 . 7 Coolant temperature at the stagnation point as a function of time for 3 different coolant inlet velocities (300mA beam current)

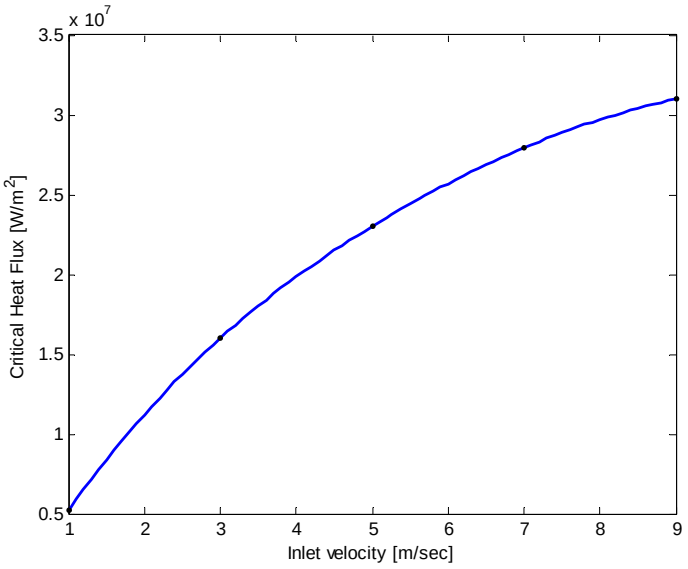

Figure 5 . 8 Critical heat flux as a function of the coolant inlet velocity

As seen from Figures 5.6, 5.7 and 5.8, the maximum target body temperature is reached in 2 seconds for all tested inlet velocities. In case of the 3 m/sec inlet velocity, the maximum temperature is 829.17^{o}K, but, the critical heat flux at the same inlet velocity is computed to be 1.59×10^{7} W/m^{2}. For an incident heat flux of 1.8×10^{7} W/m^{2} it can be inferred that boiling transition is possible for coolant inlet velocities less than about 3.5 m/sec.

5. Conclusion

Target cooling in the wide beam x-ray source is a major design consideration due to the use of high beam current as compared to conventional x-ray sources. Passive cooling or rotating target geometry is not feasible for this wide beam source design and therefore an active cooling system is required to satisfy the minimum operation time of about 20 sec for a successful DEI scan. Previous studies of target cooling by liquid nitrogen cooled cold fingers

determined that cooling by conduction cannot provide better than 4 sec operation with a 300 mA beam current [15], which is not sufficient to obtain the required DEI scan.

In this study, an active cooling system is proposed based upon an impinging water jet at atmospheric pressure. The prototype target design has been simulated using the finite element code ANSYS CFX. Simulation results have shown that impinging jet cooling, with coolant inlet velocities in excess of 3.5 m/sec allows for steady state operation while satisfying all thermal design constraints.

Notation

D : Surface diameter, m

d : Jet exit diameter, m

S : Exit-to-impingement distance, m

Re : Reynolds number

Nu : Nussle number

Pr : Prandtl number

q : Heat flux

ρ : Specific density, kg/m^3

h_{hg} : Latent heat of vaporization, J/kg

σ : Surface tension, N/m

u : Exit velocity of liquid jet, m/s

Cp : Specific heat at constant pressure, J/(kg K)

T : Temperature, K

Subscript

v : Vapor

l : Liquid

sat : Saturation

CHF : Critical heat flux

Reference

[1] Chang H. Kim, Mohamed A. Bourham, J. Michael Doster, A wide beam x-ray source suitable for diffraction enhanced imaging application, Nuclear Instrument and Method in Physics Research A 566: 713-721 ,2006.

[2] Chapman D, Thomlinson W, Johnston RE, et al. Diffraction enhanced x-ray imaging, Phys. Med. Bio. 42: 2015-2025, 1997.

[3] Zhong Z., Thomlinson W., Chapman D., Sayers D. Implementation of Diffraction Enhanced Imaging at the NSLS and APS, Nuclear Instrument and Method in Physics Research A 447: 556-568, 2000.

[4] Jerrold T. Bushberg et al, The Essential Physics of Medical Imaging, 2nd ed., Lippincott Williams & Wilkins (2002), Baltimore Maryland

[5] Joseph Selman, The fundamentals of imaging physics and radiobiology, Chares C Thomas Publisher, 2000.

[6] Martin, H., 1977, ‘‘Heat and Mass Transfer Between Impinging Gas Jets and Solid Surfaces,’’ Adv. Heat Transfer, 13, pp. 1–60.

[7] Mills AF. Heat Transfer. Second Edition. New Jersey: Prentice Hall, 1999.

[8] Jambunathan, K., Lai, E., Moss, M. A., and Button, B. L., 1992, ‘‘A Review of Heat Transfer Data for Single Circular Jet Impingement,’’ Int. J. Heat Fluid Flow, 13, pp. 106–115.

[9] D H Lee and Jeonghoon Song, “The Effects of Nozzle Diameter on Impinging Jet Heat Trasfer and Fluid Flow”, Transactions of the ASME, vol. 126, 2004

[10] Viskanta, R., 1993, ‘‘Heat Transfer to Impinging Isothermal Gas and Flame Jets,’’ Exp. Therm. Fluid Sci., 6, pp. 111–134.

[11] Zhen-Hua Liu, Tie-Feng Tong, and Yu-Hao Qiu, 2004, Critical heat flux of steady boiling for subcooled water jet impingement on the flat stagnation zone, J. Heat Transfer, vol 126, Issue 2, pp. 179-183

[12] Beitelmal, A. H., Saad, M. A., and Patel, C. D., 2000, ‘‘The Effect of Inclination on the Heat Transfer Between a Flat Surface and an Impinging Two-Dimensional Air Jet,’’ Int. J. Heat Fluid Flow, 21, pp. 156–163.

[13] Womac DJ, Ramadhyani S and Incropera FP. “Correlating Equations for Impingement Cooling of Small Heat Sources With Single Circular Liquid Jets,” Transactions of the ASME, vol. 115, 1993.

[14] Monde, M., and Kotto, Y., 1978, ‘‘Bournout in a High Heat-Flux Boiling System With an Impingement Jet,’’ Int. J. Heat Mass Transfer, 21, pp. 295–305.

[15] C.H. Kim, A study of an areas X-ray source for diffraction enhanced imaging for clinical and industrial application, M.S. Thesis, NC State University, August 2004.

Chapter 6 Conclusions and Recommendations for Future Work

1 Conclusion

Computational studies of a prototype concentric filament area x-ray source with a tilted stationary target made of a molybdenum layer sintered on oxygen-free copper have shown the capability to produce target flux comparable to a synchrotron source. Electron trajectories and their distribution on the target were computed for two different configurations. The focusing cup at –60kVp and the filament biased by –12Vp produces a uniform distribution, however, there was a loss of electron population. With both the filament and the focusing cup at –60kVp, the electrons are well focused on the target, which results in less background radiation. Thermal management was investigated over a range of beam current between 3mA to 3A. The maximum target surface temperature using a contact liquid nitrogen cold finger with a 3A beam current exceeded the melting point of copper (1357^{o}K) in 70 seconds. Using an invaded target configuration at 3A beam current, with liquid nitrogen circulating inside the target, the maximum target surface temperature reaches 325^{o}K in 10 seconds, and remains unchanged thereafter. The characteristic x-rays $K_{\alpha 1}$, $K_{\alpha 2}$ and $K_{\beta 1}$ of the molybdenum target have been investigated for aluminum and beryllium window materials. Simulation results have shown that reduction of the Bremsstrahlung is better with aluminum window as compared to beryllium. The $K_{\alpha 1}$ x-ray flux for a beam current of 3A with 0.01mm aluminum window is 2.92×10^{10}ph/mm^2/sec, which is two orders of magnitude less than a synchrotron source, however, area magnification to 100cm^2 for a scaled-up industrial system could provide the target flux required for DEI applications. An industrial scale device operating at 3A beam current and a Molybdenum target area of 100cm^2 provides a target flux of 4.808×10^{11}ph/mm^2/sec, which is comparable to a synchrotron source target flux. The use of a

beryllium window would allow for higher flux at lower beam currents, with the advantage of having a thicker window rather then a thin aluminum one to sustain high vacuum requirements; however, plasma sputter deposition techniques could be used to deposit thin layer of beryllium on high vacuum viewing windows.

Because electron distribution on the actual focal area produced non-uniformity on the final DEI image, as well as the raw images, MATLAB protocols 'codes' were written to simulate effects of the actual focal area distribution on the final DEI images. The developed protocols include the Si [333] crystal monochromator response, x-ray optics on the designed phantom and the response of the Fuji BAS2500 image plate. Two DEI image sets were obtained using two different electron distributions on the target. The first image set was obtained from applying same electron distribution to the lower and higher side images. The DEI absorption images contained similar intensity distribution through the whole images, which is a natural outcome based on the expression of the absorption image. In case of the refraction image, some regions showed similar intensity shapes with blurring at the edge of nylon cylinder. However, the image is more uniform compared to the absorption image. The second simulation was performed with different electron distributions, one for the higher side image and one for the lower side image. The DEI absorption image shows some image overlap, with increased non-uniformity on the refection image but decreased edge blurring. Refraction images in both cases remained at good resolution for the aluminum oxide region, which simulates the calcification inside the nylon cylinder.

To investigate the effect of individually-powering the filaments on the trajectories and electron distribution on the target, the three concentric filaments assembly was tested, via computational simulation, and compared to the floating filament concept. The primary

simulation shows that the outer filament provides repulsion force on the electrons and reduces losses if it would be kept at the same potential of the filament cup at -60kVp, and that a lower voltage on the inner filament helps to disperse electron trajectories to the target. For the quantitative comparison, the standard deviation and the peak-to-average ratio were used as measures of the optimized independent filament performance. The final simulation results showed that the option of having the outer filament at -60kVp, the middle at -48kVp and the inner at -40kVp, results in minimum standard deviation and peak-to-average ratio, and achieved 100% of electron utilization. Therefore, wiring of the filaments in the filament cup should be independent to achieve better utilization on the target and near uniform distribution. Filaments may use the same power supply with potential dividers to provide the required voltage to each filament from one common power supply.

A change was implemented in the target cooling to use a jet with water as the coolant to eliminate the use of liquid nitrogen was investigated. This active cooling system using an impinging coolant jet at atmospheric pressure maximizes the convective heat transfer of the coolant. The designed target has been simulated using finite element method of the ANSYS CFX code, Simulation results have shown that the impinging jet cooling, with coolant inlet velocity of 3.5 m/sec, provides sufficient operation time and that the target temperature is below the melting point. For an engineering margin, an inlet velocity higher then 3.5 m/sec should be considered to ensure safe operation.

2 Recommendations for future work

Based on the computational studies of the proof-of-principle model, which uses a 2.79cm diameter molybdenum target, it is important to complete a study on an upscale device

design in which area magnification should be considered. An area magnification by a factor of 16.242, 11.28cm target diameter provides the necessary photon flux comparable to a synchrotron source. This upscaling is a 4.04 scale factor to be applied to the geometry of the proof-of-principle design.

The size and location of the circular concentric filaments should be modified for an upscaled model, with proper individual electric power to each filament to maximize particle flux and optimize electron distribution uniformity on the target. It may be more advantageous to increase the number of circular filament to 4 or 5 to obtain better distribution by controlling the electron trajectories, and hence decreasing thermal loading on each filament, improving fine control of electron trajectories, and providing more uniform focal area distribution on the target.

It is also recommended to increase the number of the jet nozzles for better active cooling of the target. The coefficient of convective heat transfer decreases as the diameter of the impingement surface increases, and therefore, using an array of jet nozzle is recommended. The correlation of convective jet heat transfer coefficient with an array of round jet nozzles has been investigated by Krötzsch (1968). An array of jet nozzles will form a secondary stagnation point with adjacent nozzle, and hence an investigation of these stagnation points will be required for preventing local heat overloading in a multi-nozzle jet system.

Appendices

Appendix A. SIMION geometry code for electron trajectory simulation

The following code was written with the script of SIMION geometry.

```
PA_Define(56,71,71,planar,non-mirrored)

Locate(39,35,31,1,110,0,0)          ;target code 20 degree angle
{
Electrode(1) {Fill{within{cylinder(0,0,0,18,18,10)}}}
}

Locate(4,35,35,1,90,0,0) ;backing plate
{
Electrode(2){Fill{within{cylinder(0,0,0,16,16,4)} notin {cylinder(0,0,0,15,15,3)}}}
}

Locate(3,35,35,1,90,0,0)
{
Electrode(3) ;Filament # 3
{
Fill{within{cylinder(0,0,0,12.0625,12.0625,1)} notin {cylinder(0,0,0,11.0625,11.0625,1)}}
}
Electrode(4) ;Filament # 2
{
Fill{within{cylinder(0,0,0,8.2067,8.2067,1)} notin {cylinder(0,0,0,7.2067,7.2067,1)}}
}
Electrode(5) ;Filament # 1
{
Fill{within{cylinder(0,0,0,4.45,4.45,1)} notin {cylinder(0,0,0,3.45,3.45,1)}}
}
}
```

Appendix B. MCNP5 code for x-ray flux calculation

The following code was followed the structure of MCNP5. The code was used for x-ray flux calculation with varying x-ray window thickness of Al and Be.

```
C cell card
1 1 -8.92 -1 10 -11
2 2 -10.208 (1:-10:11) -1 9 -10
3 3 -7.874 (1:-9:11) -4 -5 6
4 0 -2 8 -12 #1 #2 #3
5 3 -7.874 (2:-8:12) -3 8 -12
6 3 -7.874 (3:-8:12) -17 3 -12 19
7 3 -7.874 (17:-3:12:-19) -17 12 -13
8 3 -7.874 (3:-8:12) -17 3 8 -18
9 4 -2.7 (17:-3:-8:18) -17 7 -8 $ Al or Be window
10 5 -0.00129 -14 15 -16 #1 #2 #3 #4 #5 #6 #7 #8 #9
11 0 (14:-15:16)

C surface card
1 1 cz 1.74625
2 cz 7.62
3 cz 7.9248
4 cy 1.5875
5 py -2.5
6 py -5.4
7 pz -16.7688 $ lower location of the window surface
8 pz -16.6688 $ higher location of the window surface
9 1 pz -.1
10 1 pz 0
11 1 pz 5.715 $ target body
12 pz 16.6688
13 pz 18.8913 $half inch
14 cz 12
15 pz -20
16 pz 20
```

```
17 cz 10.16
18 pz -14.4463
19 pz 14.4463

mode p e
imp:p 1 1 1 1 1 1 1 1 1 1 0
imp:e 1 1 1 1 1 1 1 1 1 0 0
sdef erg=0.06 sur=5 pos=0 -2.5 0 rad=d1 par=3 dir=1 ara=9.93147 vec=0 1 0
si1 2
sp1 -21 1
m1 29000.02p 1
m2 42000.02p 1
m3 26000.02p 1
m4 13000.02p 1
m5 7000.02p 0.78 8000.02p 0.22
tr1 0 0 0 1 0 0 0 .3826 -.92388 0 .92388 .3826 1
e0 1.0e-5 9999I 0.1 $Ka2 0.01737 Ka1 0.01748 Kb1 0.01961
f2:p 15 $ surface flux at outside of window
nps 100000000
prdmp    100000000 100000000 1 1
print
```

Appendix C. Matlab code for modeling DEI images of dual cylinder objects.

The following code was created using Matlab 7.1. The code was used to obtain the raw images on the DEI experiment and applying the DEI algorithm for the final refraction and absorption image.

C.1 The DEI images based on the wide beam x-ray source

```
% 1. Load the electron distribution result from SIMION.

d = 14;      % array number
load('data_60_48_40.mat');
eout = surface_distribution(data,d);

% 2. Maching the loaded data to actual size of target

r = 1.7;      % target radius    unit : cm
d = d/2;      % data number
e_bin = r / d;
[ex,ey] = meshgrid(-r:e_bin:r,-r:e_bin:r);

% 3. Data fitting for smaller bin size

en_bin = e_bin / 10; % unit : cm
[ex_n,ey_n] = meshgrid(-r:en_bin:r,-r:en_bin:r);
emout = interp2(ex,ey,eout,ex_n,ey_n,'spline');


% 4 . Select the field of view with appying target angle

x_l = 0.8; % unit : cm
t_angle =(90 - 22.5) * (pi/180); % unit : radian
y_l = x_l / cos ( t_angle ) ;
x_half = y_l / 2; % unit : cm
y_half = x_l / 2; % unit : cm
```

```
x_pixel = ( round( x_half / en_bin ) );
y_pixel = ( round( y_half / en_bin ) );
emout = emout';

[x_pos,y_pos] = maximum_area(emout,x_pixel,y_pixel);
x_min = x_pos - x_pixel;
y_min = y_pos - y_pixel;
x_max = x_pos + x_pixel;
y_max = y_pos + y_pixel;
mod_out = emout(x_min:x_max,y_min:y_max);

figure(3)
imagesc(mod_out)
title('Maximum Area')

% The results shows the data for the window. It is required new mesh grid for the appying
rocking curve.

x_leng = (x_max - x_min);
x_length = (x_leng * en_bin )/2;
y_leng = (y_max - y_min);
y_length = (y_leng * en_bin )/2;
x_en_bin = x_length / ( y_pixel );

[x_mod,y_mod] = meshgrid(-x_length:x_en_bin:x_length,-y_length:en_bin:y_length);
[x_mod_or,y_mod_or] = meshgrid(-x_length:en_bin:x_length,-y_length:en_bin:y_length);
mod_out_s = interp2(x_mod_or(1,:),y_mod_or(:,1),mod_out',x_mod,y_mod,'spline');
mod_out_s = mod_out_s';

figure(4)
imagesc(mod_out_s)
axis square;

% 5. Applying the rocking curve
```

```
% mod_out_s is the electron distribution at the view from the window. Therefore, the rocking curve should apply to this distribuiton. Field of View is 0.8 * 0.8 cm The pixel number : 39 * 39
angle_in = -10.0e-6:0.1e-6:10.0e-6;
y = rocking_fit_mod(angle_in);

figure(5)
stem((angle_in*10^6),y)
title('Rocking Curve of Si[333] with Mo Ka1 energy ')
xlabel('Angle [ micro radian ]')
ylabel('Reflectivity')

% The generated rocking curve is 1 Dimentional data set. In this simultion, it is required to obtain 2D data. The 2D guassian function was already have. So. the sigma is required for the function. The FWHM = 2.354 sigma.

num_angle = size(angle_in);
num_ang = num_angle(1,2);
half_ref = max(y)/2;
k = 0;
for i = 1 : num_ang
        temp = y(i);
        if temp >= half_ref
                k = k +1;
        else
                k = k + 0;
        end
end

rocking_bin = 0.5e-6; % unit : radian
FWHM = k * 0.1e-6;
sigma = FWHM / 2.354;
[x2,y2] = meshgrid(-10.0e-6:rocking_bin:10.0e-6,-10.0e-6:rocking_bin:10.0e-6);
yg2 = gauss_function(x2,y2,sigma);
```

```
[xp_gau,yp_gau,max_gau] = finding_maximum_position_2D(yg2);
fact = max(y) / max_gau;
mod_gauss_2D = yg2 * fact;

% 2D gaussian Distribution was generated. x2 and y2 is the mesh for the distribution

figure(6)
mesh((x2)*10^6,(y2)*10^6,mod_gauss_2D)
title('2D Rocking Curve');
xlabel(' Angle [ mirro radian ]')
ylabel(' Angle [ micro radian ]')
zlabel(' Reflectivity ' )

x_i_min = -0.4 / 100; % unit m
x_i_max = 0.4 / 100;    % unit m
y_i_min = -0.4 / 100; % unit m
y_i_max = 0.4 / 100; % unit m
i_pixel = 50.0e-6; % unit m
post_i_pixel = (0.8/100)/y_leng;

[x_mod,y_mod] = meshgrid(x_i_min:post_i_pixel:x_i_max,y_i_min:post_i_pixel:y_i_max);
[x_mod_or,y_mod_or] = meshgrid(x_i_min:i_pixel:x_i_max,y_i_min:i_pixel:y_i_max);
out_image = interp2(x_mod,y_mod,mod_out_s,x_mod_or,y_mod_or,'spline');

figure(7)
imagesc(out_image)
title('Actual size of electron distribution')
axis square;
axis off;

% 2D gaussian shows in the range of -10 micro radian to 10 micro radian, this can be
changed the dimention to meter, which is -2 micro m to 2 micro m.
r_x_min = -2.0e-6; % unit : m
r_x_max = 2.0e-6; % unit : m
```

```
r_y_min = -2.0e-6; % unit : m
r_y_max = 2.0e-6; % unit : m
s_out_image = sum ( sum ( out_image ) );
m_out_image = ( out_image / s_out_image );

figure(8)
surf(m_out_image)
title('Nomailzed Electron Distribution');

% Appying two distribuiton to lower and higer side image
m_out_image_h = m_out_image;
m_out_image_l = m_out_image;
beam = 0.3 * 10; % Applying beam current for image    Unit : Ampare

% 6. Detector plate setup
y = [-0.4 0.4];
z = [-0.4 0.4];
pixel = 161;
inten_o_h = m_out_image_h * beam * 6.25e18 * 0.686 * 0.3868 ;
inten_o_l = m_out_image_l * beam * 6.25e18 * 0.686 * 0.3868 ;
effect_length = 21;
FWHM = 0.0138;

% 7. DEI simulation setup

% Position
s_to_obejct = 40;
o_to_detect_radio = 5;
o_to_detect = 90;

% Material Properties, linear attenuation coeffient and refractive index
mu_air = 1.47e-3;
mu_tiss = 0.616;
mu_car = 11.77;
```

```
del_tiss = 8.56e-7;
del_car = 2.467e-6;
del_air = -0.00029;

% Object properties
D_tiss = 0.6351; % unit : cm
D_car = 0.05;        % unit : cm
L_car = 0.4;
car_location = -0.15875;

% Lower and higher side scanning position of Rocking curve
lower_angle = -2;
higher_angle = 2;

r_tiss = D_tiss / 2;
r_car = D_car / 2;
L_half_car = L_car / 2;
[mid_y,mid_z]=mid_point(y,z,pixel);

% Line spread function from the detector plates
sigma_x = 0.00317;
sigma_y = 0.00027;

% x-ray flux response from MCNP simulation
initial_single_flux = 1.2e-8; % unit : # / mm2 sec k alpha one flux of Mo
pixel_length = 50.0e-3; % unit : mm
single_flux = initial_single_flux * ( pixel_length )^2;
i_source =(source_setup(sigma_x,sigma_y,pixel,y,z))*single_flux;

% 8. Lower side image
lower_raw_1 =
Dual_DEI_2(mid_y,mid_z,r_tiss,r_car,L_half_car,car_location,inten_o_l,s_to_obejct,o_to_d
etect,del_tiss,del_car,mu_air,mu_tiss,mu_car,lower_angle,pixel);
lower_with_source = imfilter(i_source,lower_raw_1,'circular','conv');
```

```
lower_image_psf = point_spread_f(lower_with_source,effect_length,FWHM);
lamda_l = lamda_f_m(lower_image_psf,pixel);
[lower_image,n_l] = add_noise_m(lower_image_psf,lamda_l,pixel);


figure(9)
imagesc(lower_image)
colormap('gray')
title('Lower side raw image');
axis square;
axis off;

% Appying detectro response
S = 4000 ;
L = 5 ;
G = 2^16;

I_plate_lower = plate_intensity(lower_image,S,L,G);
I_log_lower = log(I_plate_lower);
I_plate_max = plate_intensity(14000,S,L,G);
I_log_max = log(I_plate_max);
I_plate_min = plate_intensity(0.1,S,L,G);
I_log_min = log(I_plate_min);

figure(10)
clims = [I_log_min I_log_max];
imagesc(I_log_lower,clims)
colormap('gray')
title('Lower side image plate reading');
axis square;
axis off;

% 9. Higher side image
higher_raw_1 =
```

```
Dual_DEI_2(mid_y,mid_z,r_tiss,r_car,L_half_car,car_location,inten_o_h,s_to_obejct,o_to_d
etect,del_tiss,del_car,mu_air,mu_tiss,mu_car,higher_angle,pixel);
higher_with_source = imfilter(i_source,higher_raw_1,'circular','conv');
higher_image_psf = point_spread_f(higher_with_source,effect_length,FWHM);
lamda_h = lamda_f_m(higher_image_psf,pixel);
[higher_image,n_h] = add_noise_m(higher_image_psf,lamda_h,pixel);

figure(11)
imagesc(higher_image)
title('Higher side raw image');
colormap('gray')
axis square;
axis off;

I_plate_higher = plate_intensity(higher_image,S,L,G);
I_log_higher = log(I_plate_higher);

figure(12)
clims = [I_log_min I_log_max];
imagesc(I_log_higher,clims)
title('Higher side image plate reading');
colormap(gray)
axis square;
axis off;

% 10. Generation of absorption and refraction images
[absorption,refraction] =
DEI_Algorithm(higher_image,lower_image,pixel,higher_angle,lower_angle);

figure(13)
imagesc(absorption)
title('Absorption');
axis square;
colormap(gray)
```

```
axis off;

figure(14)
imagesc(refraction)
title('Refraction');
axis square;
colormap(gray)
axis off;
```

C.2 Function of DEI algorithm

```
function [absorption,refraction] = DEI_Algorithm(higher,lower,pixel,angle_h,angle_l)
for ( i = 1 : pixel )
      for ( j = 1 : pixel )
            num_absorp = lower(i,j) * derivation(angle_h) - higher(i,j) * derivation(angle_l);
            deno_absorp = lower_fitting(angle_l) * derivation(angle_h) -
lower_fitting(angle_h) * derivation(angle_l);
            absorption(i,j) = num_absorp / deno_absorp;
            num_refraction = higher(i,j) * lower_fitting(angle_l) - lower(i,j) *
lower_fitting(angle_h);
            deno_refraction = lower(i,j) * derivation(angle_h) - higher(i,j) *
derivation(angle_l);
            refraction(i,j)= num_refraction / deno_refraction;
            end
end
```

Appendix D. ANSYS simulation results

The ANSYS products, ICEM CFD and ANSYS CFX, were used for the computational fluid dynamics model for the heat removal simulations.

D.1 Target design with Solidworks

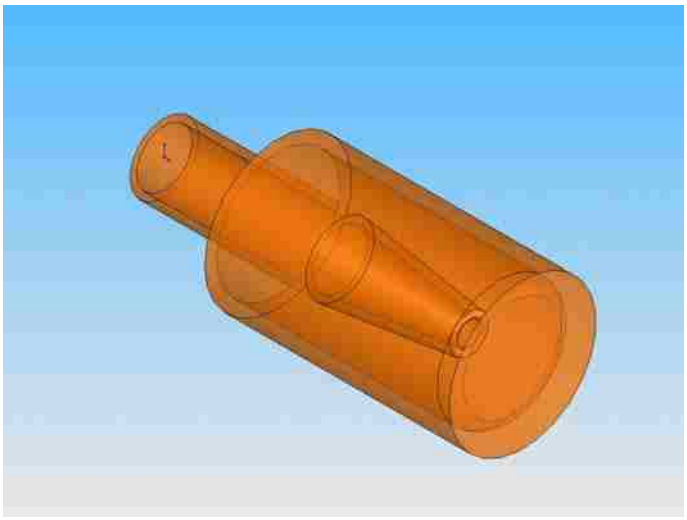

Figure A . 1 Target body design

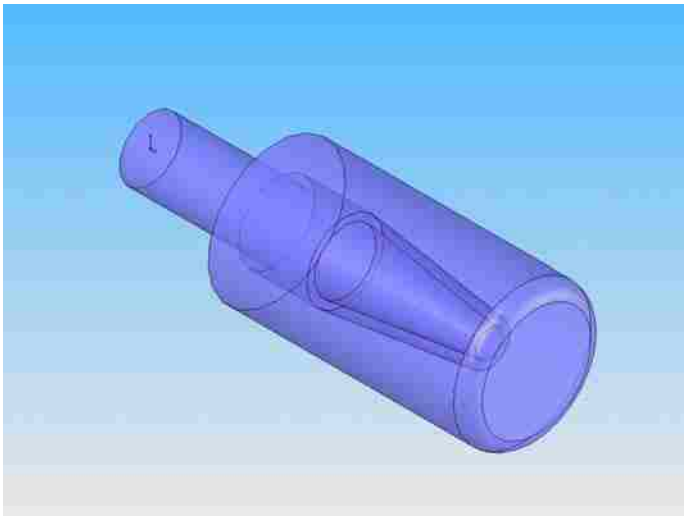

Figure A . 2 Coolant channel design

D.2 ICEM CFD result views for initial mesh and prism added mesh

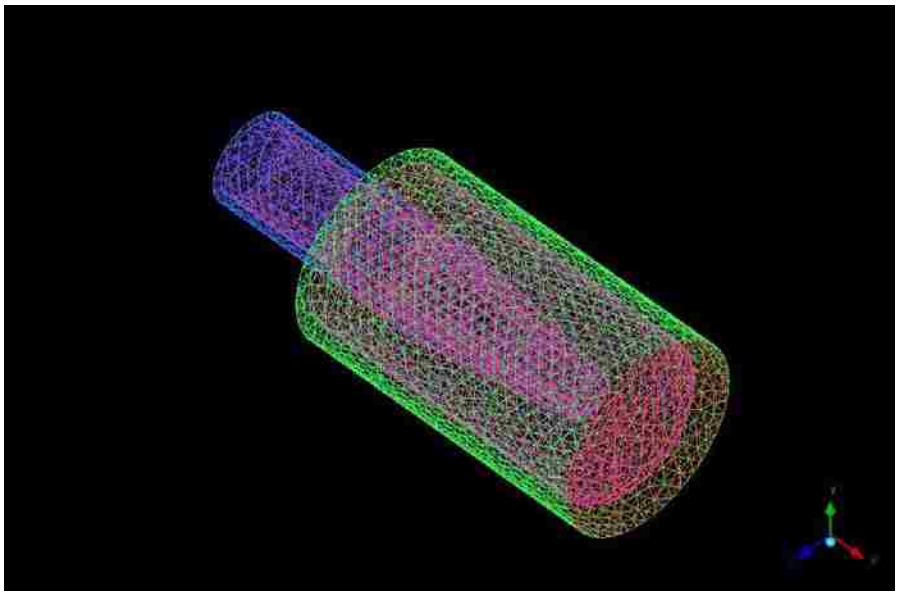

Figure A . 3 Isometric view of initial mesh

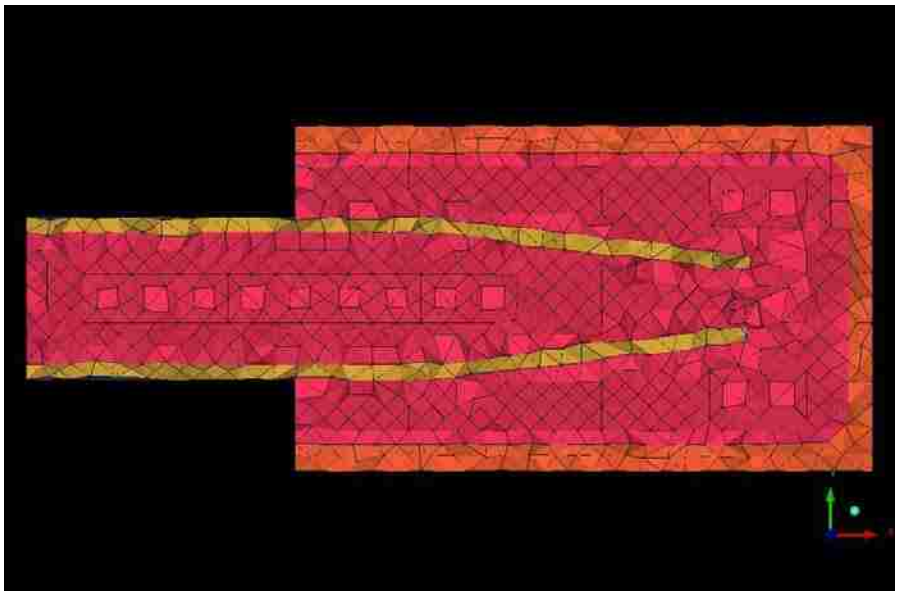

Figure A . 4 Side view of initial mesh

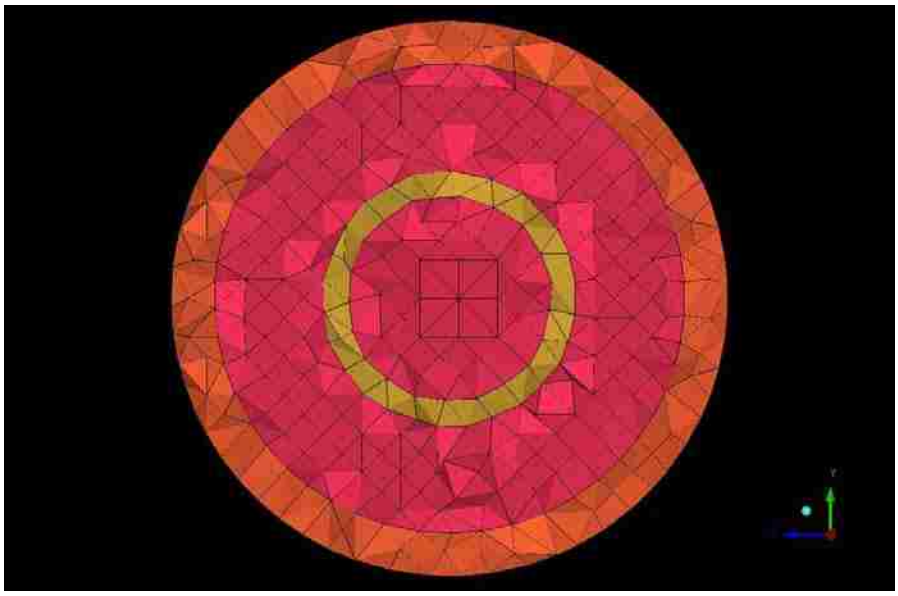

Figure A . 5 Top view of initial mesh

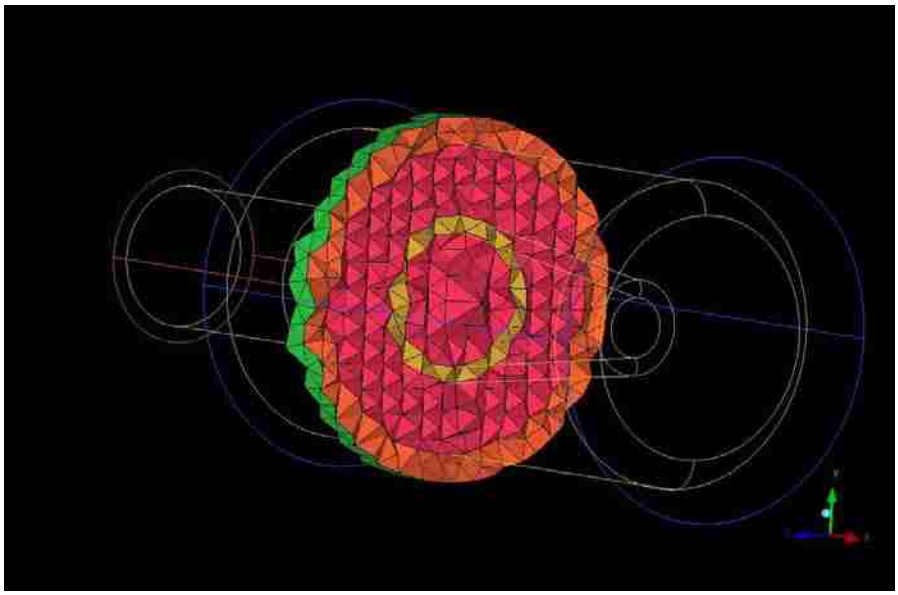

Figure A . 6 Middle cut view of initial mesh

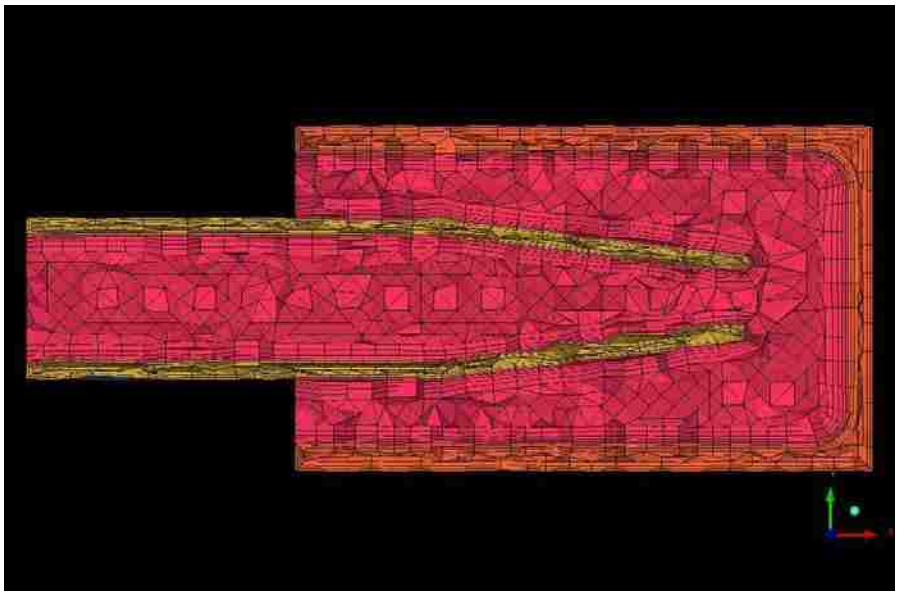

Figure A . 7 Side view of prism mesh added

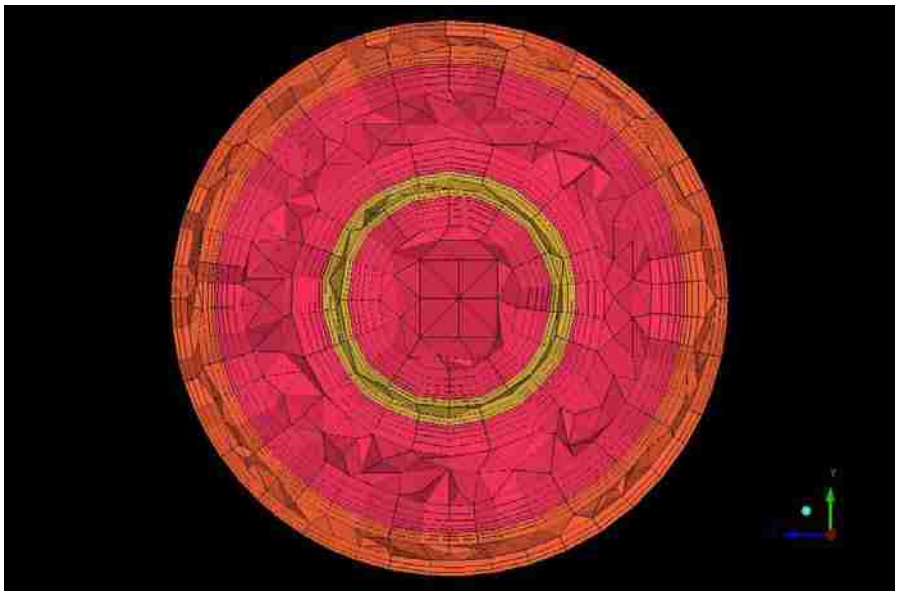

Figure A . 8 Top view of prism mesh added

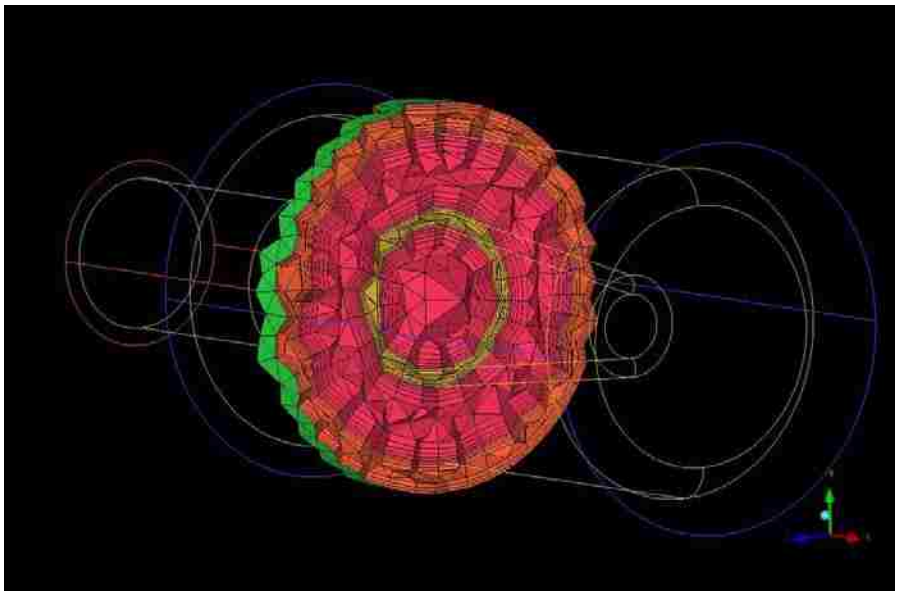

Figure A . 9 Middle cut view of prism mesh added

D.3 ANSYS CFX result views

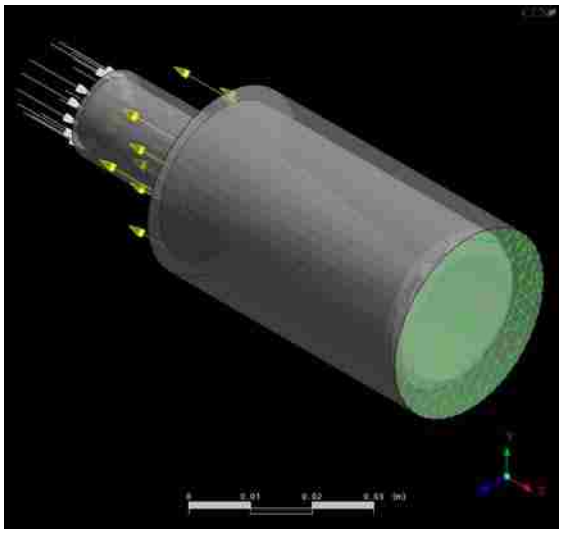

Figure A . 10 ANSYS CFX PRE view

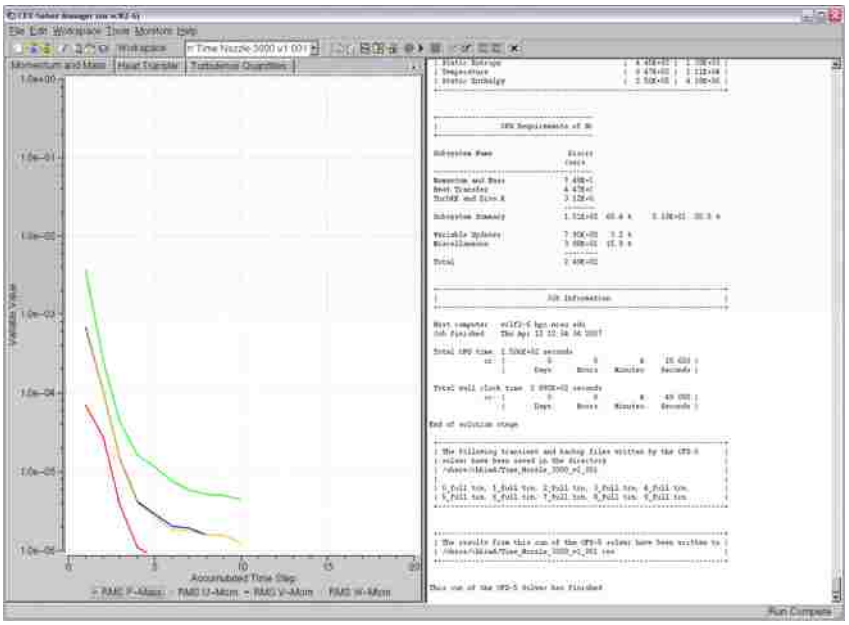

Figure A . 11 ANSYS CFX Solver view of the convergence history plot for Momentum and Mass

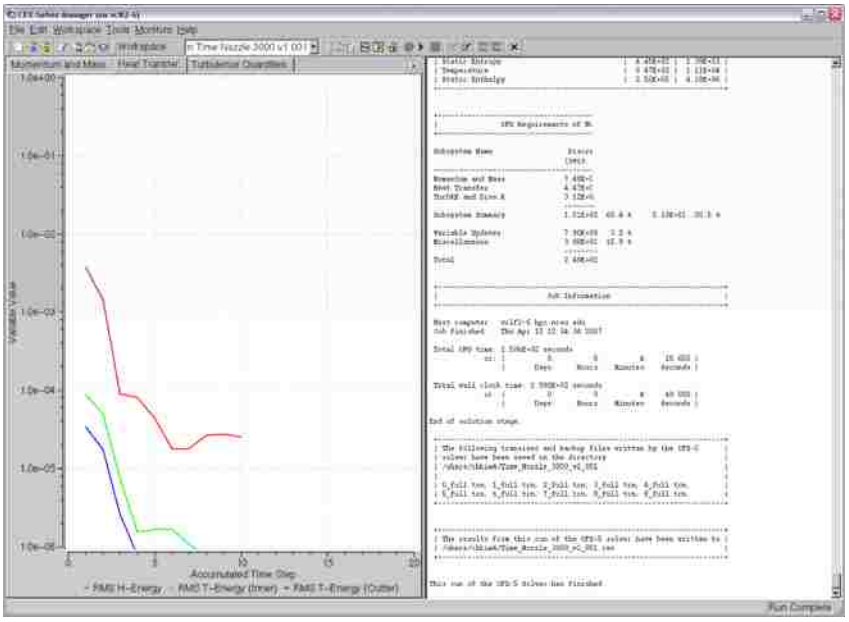

Figure A . 12 ANSYS CFX Solver view of the convergence history plot for Heat Transfer

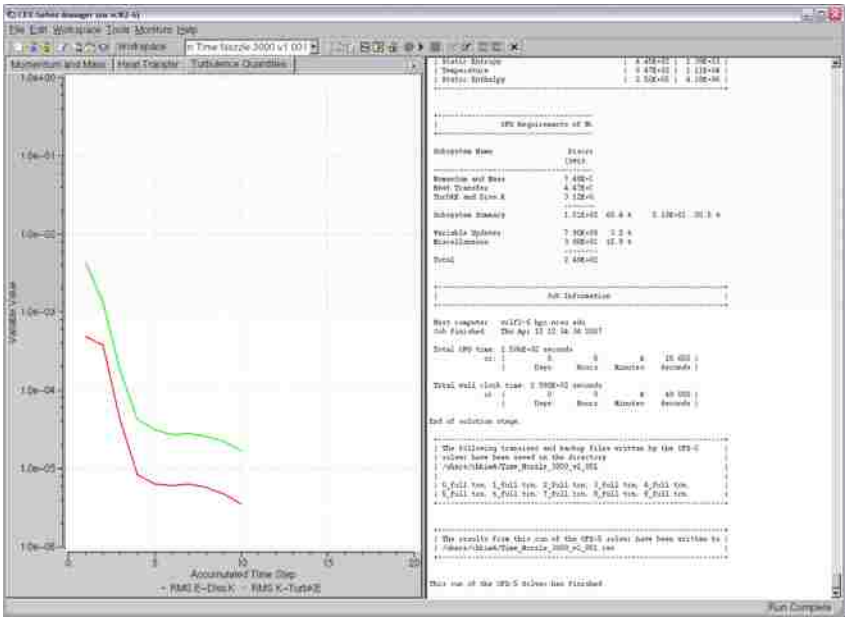

Figure A . 13 ANSYS CFX Solver view of the convergence history plot for Turbulence Quantities

D.4 Additional ANSYS CFX Transient results

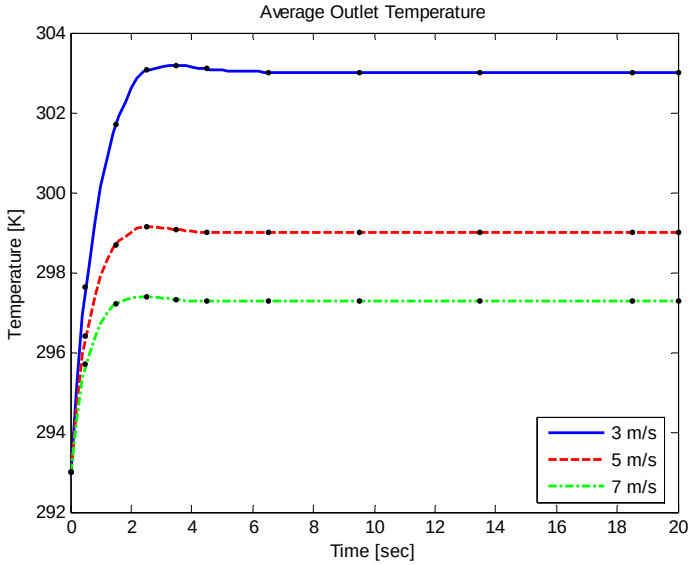

Figure A . 14 Average outlet temperature with varying inlet velocity at 300 mA beam current

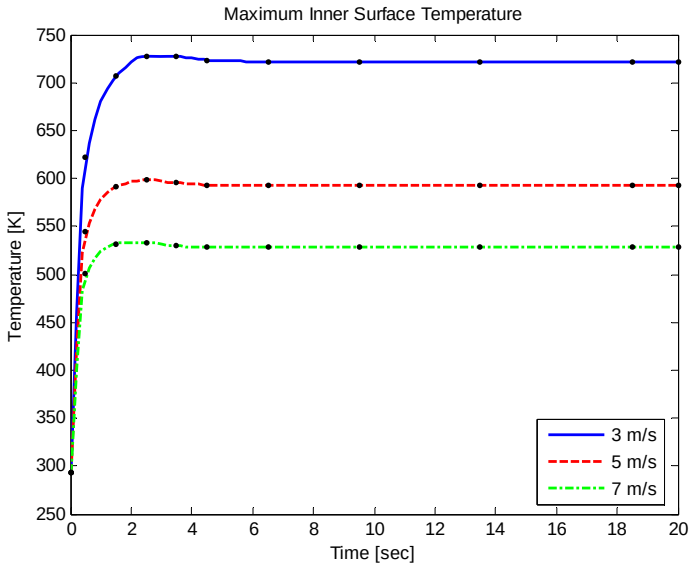

Figure A . 15 Maximum inner surface temperature with varying inlet velocity